MNRAS **000**, 1–24 (2019) Preprint 15 October 2019 Compiled using MNRAS LATEX style file v3.0

Massive Low Surface Brightness Galaxies in the EAGLE Simulation

Andrea Kulier[1,2]⋆, Gaspar Galaz[1], Nelson D. Padilla[1], James W. Trayford[2]
[1]*Instituto de Astrofísica, Pontificia Universidad Católica de Chile, Av. Vicuña Mackenna 4860, Santiago, Chile*
[2]*Leiden Observatory, Leiden University, P.O. Box 9513, NL-2300 RA Leiden, The Netherlands*

15 October 2019

ABSTRACT

We investigate the formation and properties of low surface brightness galaxies (LSBGs) with $M_* > 10^{9.5}\mathrm{M}_\odot$ in the EAGLE hydrodynamical cosmological simulation. Galaxy surface brightness depends on a combination of stellar mass surface density and mass-to-light ratio (M/L), such that low surface brightness is strongly correlated with both galaxy angular momentum (low surface density) and low specific star formation rate (high M/L). This drives most of the other observed correlations between surface brightness and galaxy properties, such as the fact that most LSBGs have low metallicity. We find that LSBGs are more isolated than high surface brightness galaxies (HSBGs), in agreement with observations, but that this trend is driven entirely by the fact that LSBGs are unlikely to be close-in satellites. The majority of LSBGs are consistent with a formation scenario in which the galaxies with the highest angular momentum are those that formed most of their stars recently from a gas reservoir co-rotating with a high-spin dark matter halo. However, the most extended LSBG disks in EAGLE, which are comparable in size to observed giant LSBGs, are built up via mergers. These galaxies are found to inhabit dark matter halos with a higher spin in their inner regions ($< 0.1r_{200c}$), even when excluding the effects of baryonic physics by considering matching halos from a dark matter only simulation with identical initial conditions.

Key words: galaxies : formation — galaxies : evolution — galaxies : structure

1 INTRODUCTION

Low surface brightness galaxies (LSBGs) are galaxies whose disks are at least one magnitude fainter than the typical sky brightness (Impey & Bothun 1997). The exact surface brightness value delimiting this category of objects varies throughout the observational literature, but a common definition is galaxies having a central disk surface brightness fainter than 22 to 23 mag/asec^2 in the B-band (Impey et al. 2001). These galaxies are challenging to observe due to their faintness, but surveys of their population in the local Universe suggest that they constitute most of the total number density of low-mass galaxies (Dalcanton et al. 1997a), and $\sim$ 10% of the cosmic baryon budget (Minchin et al. 2004). At higher masses, so-called 'giant' LSBGs like Malin 1 (Bothun et al. 1987) and UGC1382 (Hagen et al. 2016) have the largest known disks in the Universe, whose extreme sizes potentially challenge our understanding of galaxy assembly (Galaz et al. 2015; Boissier et al. 2016). Thus LSBGs are an important but still poorly understood component of the overall galaxy population.

A number of authors have found that the properties of LSBGs are statistically different from those of high surface brightness galaxies (HSBGs), likely indicating a different formation or evolution scenario for LSBGs. LSBGs have been found to live in low-density environments and to have a deficit of nearby neighbors (Bothun et al. 1993; Mo et al. 1994; Rosenbaum & Bomans 2004; Rosenbaum et al. 2009; Galaz et al. 2011; Du et al. 2015), implying that isolation may be necessary for either LSBG formation or survival. LSBGs have also been measured to have low star formation rates (van der Hulst et al. 1993; van den Hoek et al. 2000) and low metallicities (McGaugh 1994; de Blok & van der Hulst 1998; Burkholder et al. 2001). Some works find that the star formation rates of LSBGs are not unusual relative to their stellar mass (Galaz et al. 2011, and references therein), but that their richness in HI implies low star-formation efficiency (Wyder et al. 2009; Leisman et al. 2017). Additionally, LSBGs have been reported to be highly dark matter dominated (de Blok et al. 1996; Pickering et al. 1997; Lelli et al. 2010), which is thought to prevent bar formation that

⋆ E-mail: akulier@astro.puc.cl

could destroy their diffuse disks (Mayer & Wadsley 2004; see however Galaz et al. 2006).

Complicating the theoretical interpretation of these observations is the possibility that there are distinct subpopulations of LSBGs. So-called 'ultra-diffuse galaxies' (UDGs) have luminosities and stellar masses typical of dwarf galaxies, but effective radii $r_{\rm eff} \gtrsim 1.5$ kpc (van Dokkum et al. 2015a; Román & Trujillo 2017b). Unlike more massive LSBGs, observed UDGs tend to be red, dispersion-dominated, and located within clusters (Sandage & Binggeli 1984; van Dokkum et al. 2015a,b; Koda et al. 2015; Muñoz et al. 2015; Mihos et al. 2015; van Dokkum et al. 2019). However, this is at least partly due to selection effects, as UDG searches have typically focused on cluster regions. UDGs have also been discovered in less dense environments (Merritt et al. 2016; van der Burg et al. 2017; Papastergis et al. 2017), where they are more likely to be blue (Leisman et al. 2017; Zaritsky et al. 2019; Prole et al. 2019), and where some have suggested they may be even more numerous than in clusters (Román & Trujillo 2017a,b).

Giant LSBGs are also known to have peculiar features relative to their smaller counterparts. Specifically, they have bright nuclei that resemble galaxies of ordinary size, surrounded by an extremely extended faint disk (Barth 2007; Hagen et al. 2016).

Several different theoretical formation scenarios for low surface brightness galaxies exist in the literature. For UDGs, hydrodynamical zoom-in simulations have suggested that they have very bursty star formation histories, which lead to episodes of strong feedback that expel their gas and cause expansion of their stellar orbits (Di Cintio et al. 2017; Chan et al. 2018). Another proposed UDG formation channel is the expansion of dwarf galaxies with cored dark matter halos via tidal stripping and heating (Carleton et al. 2019).

One idea that has been put forth to explain both UDGs and higher-mass LSBGs is that these galaxies constitute the tail of the spin distribution of the galaxy population, forming in the most high-spin dark matter halos of a given mass (Dalcanton et al. 1997b; Jimenez et al. 1998; Amorisco & Loeb 2016; Rong et al. 2017). However, for giant LSBGs, this would require extreme halo spins possibly inconsistent with ΛCDM predictions (Boissier et al. 2016; Zhu et al. 2018). For these galaxies, it has been suggested that they build up their large outer disks via tidal disruption and accretion of small, gas-rich satellites (Peñarrubia et al. 2006; Hagen et al. 2016). Other proposed scenarios for giant LSBG formation include evolution from ring galaxies (Mapelli et al. 2008), formation in rare dark matter peaks within voids (Hoffman et al. 1992), and evolution from HSBGs via disk instabilities (Noguchi 2001).

One newly-opened avenue to exploring the formation and evolution of LSBGs is to utilize large-scale hydrodynamical cosmological simulations. Historically, limitations in computational power restricted the possibility of simulating large samples of well-resolved galaxies in their cosmological environment. However, recent years have seen the development of large simulations that produce statistically significant samples of galaxies with realistic properties, including EAGLE (Schaye et al. 2015; Crain et al. 2015), Horizon-AGN (Dubois et al. 2014; Kaviraj et al. 2017), Illustris (Vogelsberger et al. 2014; Genel et al. 2014), and IllustrisTNG (Pillepich et al. 2018).

Martin et al. (2019) studied LSBGs in the Horizon-AGN simulation, focusing on galaxies in the stellar mass range $10^8 - 10^{10}\mathrm{M}_\odot$. They found that ultra-diffuse galaxies (UDGs), defined to have r-band effective surface brightness $\langle\mu_e\rangle > 24.5$ mag/asec^2, and 'classical' LSBGs, with $23 < \langle\mu_e\rangle < 24.5$ mag/asec^2, are generally distinct in their properties. UDGs in Horizon-AGN have stellar masses $M_* < 10^9\mathrm{M}_\odot$, tend to be very gas-poor, and are typically found in dense environments such as clusters. Dynamical heating via numerous tidal interactions appears to play an essential role in their formation. 'Classical' LSBGs have properties and evolutionary histories more similar to those of HSBGs, although they formed most of their stars earlier and have lower present-day star formation.

Focusing on high masses, Zhu et al. (2018) examined the formation of a massive LSBG comparable in size to Malin 1 within the IllustrisTNG simulation. The galaxy consists of a central spheroidal component formed before $z = 0.3$ surrounded by a > 100 kpc disk of gas and more recently formed stars. Its rotation curve is also similar to what is observed for Malin 1. The authors find that the object was formed by a merger between the galaxy's main progenitor and two other massive galaxies, leading to stimulated accretion of gas from the progenitor's hot halo.

In this paper, we investigate the surface brightnesses of galaxies in the EAGLE cosmological hydrodynamical simulation, with the intent of understanding the differences between LSBGs and HSBGs. We study galaxies with $M_* > 10^{9.5}\mathrm{M}_\odot$, meaning that our focus is on 'classical' and giant LSBGs rather than UDGs. In §2, we provide a brief overview of the EAGLE simulation and describe how we compute the surface brightnesses of EAGLE galaxies, as well as other relevant galaxy parameters. In §3, we present and discuss our results, showing the correlations between galaxy surface brightness and other galaxy properties, as well as the evolutionary factors that cause a galaxy to have high or low surface brightness. Finally, in §4, we summarize our conclusions.

Throughout this paper we assume the Planck cosmology (Planck Collaboration et al. 2014) adopted in the EAGLE simulation, where $h = 0.6777$, $\Omega_\Lambda = 0.693$, $\Omega_m = 0.307$, and $\Omega_b = 0.048$.

2 METHODS

2.1 EAGLE simulation overview

EAGLE (Schaye et al. 2015; Crain et al. 2015; McAlpine et al. 2016) is a suite of cosmological hydrodynamical simulations, run using a modified version of the N-body smooth particle hydrodynamics (SPH) code GADGET-3 (Springel 2005). These modifications, described in Schaller et al. (2015a), are based on the conservative pressure-entropy formulation of SPH from Hopkins (2013), and include changes to the handling of the viscosity (Cullen & Dehnen 2010), the conduction (Price 2008), the smoothing kernel (Dehnen & Aly 2012), and the time-stepping (Durier & Dalla Vecchia 2012).

The EAGLE suite includes a number of simulation boxes with different sizes, resolutions, and subgrid physics prescriptions. In this analysis we use the reference EAGLE simulation Ref-L0100N1504, which has box size 100

comoving Mpc per side and contains 1504^3 particles each of dark matter and baryons. The dark matter particle mass is $9.70 \times 10^6 \mathrm{M}_\odot$ and the initial gas (baryon) particle mass is $1.81 \times 10^6 \mathrm{M}_\odot$. The Plummer-equivalent gravitational softening length is 2.66 comoving kpc (ckpc) until $z = 2.8$ and 0.70 proper kpc (pkpc) afterward. The subgrid physics includes prescriptions for radiative cooling, photoionization heating, star formation, stellar mass loss, stellar feedback, supermassive black hole accretion and mergers, and AGN feedback. These prescriptions and the effects of varying them are described in Schaye et al. (2015) and Crain et al. (2015).

Radiative cooling and photoionization heating is implemented using the model of Wiersma et al. (2009a). Cooling and heating rates are computed for 11 elements using CLOUDY (Ferland et al. 1998), assuming that the gas is optically thin, in ionization equilibrium, and exposed to the cosmic microwave background and a Haardt & Madau (2001) UV and X-ray background that is imposed instantaneously at $z = 11.5$. Extra energy is injected at this redshift and at $z = 3.5$ to model HI and HeII reionization respectively.

Star formation is implemented as described in Schaye & Dalla Vecchia (2008). Gas particles that reach a metallicity-dependent density threshold (Schaye 2004) become 'star-forming' and are stochastically converted into stars at a rate that reproduces the Kennicutt-Schmidt law (Kennicutt 1998). Star particles are modeled as simple stellar populations with a Chabrier (2003) initial mass function. The prescriptions for stellar evolution and mass loss from Wiersma et al. (2009b) are assumed. The stochastic feedback prescription of Dalla Vecchia & Schaye (2012) is used to model stellar feedback. The strength of the feedback is calibrated largely by adjusting the fraction of the energy lost from stars that is assumed to heat the nearby gas.

Halos that reach a mass of $10^{10}\mathrm{M}_\odot/h$ are seeded with black holes of subgrid mass $10^5\mathrm{M}_\odot/h$ at their centers by converting the most bound gas particle into a "black hole" seed particle (Springel et al. 2005). The black holes accrete gas according to the prescriptions given in Rosas-Guevara et al. (2016), and can merge with one another. Stochastic AGN feedback is implemented with an energy injection rate proportional to the black hole accretion rate. Adjustment of the fraction of lost energy assumed to heat the gas does not significantly affect the masses of galaxies due to self-regulation (Booth & Schaye 2010), and is instead calibrated to match the observed stellar mass-black hole mass relation.

Stellar feedback in the EAGLE reference simulation was calibrated to approximately reproduce the local galaxy stellar mass function (GSMF). Additionally, feedback models that resulted in overly compact galaxy sizes at $z = 0$ despite reproducing the GSMF were rejected (Crain et al. 2015). The observed galaxy size distributions used for comparison were derived from the SDSS (Shen et al. 2003) and GAMA (Baldry et al. 2012) surveys. We note that these surveys do not extend to very low surface brightness; their galaxy size distributions are derived assuming that the HSBG surface brightness distribution extends continuously to low surface brightness. Given the paucity of data in the LSBG regime, it is possible that this an incorrect assumption, and that there exist statistically distinct populations of LSBGs that are unobserved. EAGLE does produce LSBGs (as we will show in §3), but given that its galaxy size distribution depends on these calibrations, these LSBGs and the mechanisms by which they are produced are potentially only a subset of the low surface brightness Universe.

With only the subgrid physics calibrations described above, EAGLE is able to reproduce a variety of properties of the observed galaxy population. These include, among others, the $z = 0$ Tully-Fisher relation (Schaye et al. 2015), the evolution of the galaxy mass function (Furlong et al. 2015) and galaxy sizes (Furlong et al. 2017), optical galaxy colors and their evolution (Trayford et al. 2015, 2016), the SFR-M_* relation (Furlong et al. 2015), and the evolution of the star formation rate function (Katsianis et al. 2017). Galaxy and halo catalogs as well as particle data from EAGLE have been made publicly available (McAlpine et al. 2016).

2.2 Simulated galaxy sample

Galaxies in EAGLE are identified through a series of steps. First, halos are identified in the dark matter particle distribution using a friends-of-friends (FoF) algorithm with a linking length of $b = 0.2$ times the mean interparticle separation (Davis et al. 1985). Other particle types (gas, stars, and black holes) are assigned to the FoF halo of the nearest dark matter particle. The SUBFIND (Springel et al. 2001; Dolag et al. 2009) algorithm is then run over all the particles of any type within each FoF halo, in order to identify local overdensities ("subhalos"). Each subhalo is assigned only the particles gravitationally bound to it, with no overlap in particles between subhalos. The subhalo that contains the most bound particle in a FoF halo is considered to be the "central" subhalo, while any other subhalos are "satellites". The stellar and gas particles bound to a subhalo are what we consider to be an individual galaxy. Galaxy catalogs are created in this manner for a series of 29 simulation snapshots from $z = 20$ to $z = 0$.

Our initial sample of simulated galaxies consists of all the galaxies in the Ref-L0100N1504 run of EAGLE at $z = 0$ with total bound stellar mass $M_* > 10^{9.5}\mathrm{M}_\odot$. This leads to a sample of 7314 galaxies, which includes both central and satellite galaxies. We compute the surface brightnesses of these galaxies using the distribution of their bound star particles, as described in §2.3.

We additionally use the galaxy merger trees from the EAGLE catalog to investigate the evolution of galaxies with different $z = 0$ surface brightnesses. The merger trees were created from the simulation snapshots using a modified version (Qu et al. 2017) of the D-TREES algorithm (Jiang et al. 2014), which assigns each subhalo a descendant in the subsequent snapshot that contains the majority of some number of the subhalo's most bound particles. A subhalo has only one descendant but may have multiple progenitors. Each subhalo with at least one progenitor has a single "main progenitor", defined as the one with the largest mass summed across all earlier snapshots, as suggested by De Lucia & Blaizot (2007) to avoid swapping of the main progenitor during major mergers. In some cases, no descendant of a subhalo can be identified in the next snapshot, but one can be found in a later snapshot; because of this, descendants are identified up to 5 snapshots later.

2.3 Galaxy surface brightness calculation

In this subsection we describe how we obtain the surface brightness profiles and mean surface brightnesses of the galaxies in our sample. Physical distances are used in all calculations. The center of each galaxy is assumed to be at the location of its most bound particle.

Dust-free luminosities have been computed for the stellar particles of EAGLE galaxies in the SDSS *ugriz* bands as described in Trayford et al. (2015). Each star particle is assumed to be a simple stellar population with a Chabrier (2003) initial mass function and the SPH-smoothed metallicity of its parent gas particle. Its spectral energy distribution is then computed using the Bruzual & Charlot (2003) GALAXEV models. Here we compute the B band luminosity of each star particle from its u and g band luminosities using the transformation from Lupton (2005)[1]:

$$B = u - 0.8116(u - g) + 0.1313. \quad (1)$$

We compute the projected surface brightness using all the gravitationally bound star particles within 500 kpc of the galaxy's center (although only the most massive galaxies contain stellar particles this distant).

The aim of this paper is not to attempt a detailed statistical comparison with LSBG observations, but rather to investigate the properties and evolution of the population of objects that potentially could, depending on orientation, be observed as LSBGs if they existed in our Universe. Thus we compute the surface brightness for all the galaxies in our sample in the face-on orientation, with the minor axis of the galaxy oriented along the line of sight.

We first locate the 3D half-mass radius of the galaxy using all the bound star particles. We then compute the mass distribution tensor (i.e. the moment of inertia tensor) within three times this radius. The eigenvector of this tensor corresponding to the smallest eigenvalue is taken to be line-of-sight direction over which the luminosity is projected to compute the surface brightness profile.

We calculate the surface brightness profile in elliptical annuli, assuming a single axis ratio at all distances from the center derived from the remaining two eigenvalues/eigenvectors of the mass distribution tensor. We compute the local surface brightness in bins of 50 particles each. The surface brightness is converted from $L_\odot/pc^2$ to mag/asec^2 as if all galaxies were located at $z = 0.08$, the redshift of Malin 1 (Impey & Bothun 1989).

We take a simple definition of the "total" surface brightness of the galaxy: the mean surface brightness within a fixed B-band isophote of 28 mag/asec^2. This has the advantage of not requiring fitting a parametric model (such as a Sersic bulge and exponential disk), which we have found does not always accurately describe the light profiles of galaxies in the simulation. Additionally, the 28 mag/asec^2 isophote will be large for galaxies with faint disks even if they have bright nuclei (provided that the disk itself is not fainter than 28 mag/asec^2), whereas this is not necessarily the case for the half-light radius, whose position may be determined by the central bulge. However, because in EAGLE any stellar particles gravitationally bound to a galaxy are considered to be part of it, our surface brightness profiles include stellar halos and, for the most massive central galaxies, what is referred to as "intracluster light" (ICL). This faint component is generally not considered to be part of a galaxy for the purpose of computing the surface brightness, but it is difficult to identify a physically-motivated boundary between the ICL and the galaxy (see Cañas et al. 2019 for a recent attempt in cosmological hydrodynamical simulations). In EAGLE, stellar halos/ICL are built up through galaxy mergers (see §3.1), which also influence the evolution of galaxies in other ways; we therefore treat galaxies with and without significant mass growth from mergers separately when presenting our results.

To obtain an estimate of the 28 mag/asec^2 isophote that avoids local fluctuations in the surface brightness, we smooth the surface brightness profiles computed from the particles. This is done using a locally weighted linear regression (LOWESS; Cleveland 1979) of the nearest 10% of points, weighted by a tri-cube weight function:

$$w_i = (1 - |d_i|^3)^3, \quad (2)$$

where $|d_i|$ is the distance from each point in the subset to the location at which the smoothed curve is being computed, normalized so that the value lies between 0 and 1. We then take the smallest elliptical annulus at which 28 mag/asec^2 is achieved as the isophote within which we take the average surface brightness. In the remainder of this paper, we will refer to the circularized radius of this isophote as R_{28B}, and the mean surface brightness within it as $\langle\mu_B\rangle$. 124 galaxies in our initial sample do not reach a surface brightness of 28 mag/asec^2; we remove these galaxies from the sample.

We compute jackknife errors on $\langle\mu_B\rangle$, and remove those galaxies for which they are larger than 0.5 mag/asec^2. Generally this occurs for galaxies whose surface brightness profiles are nearly flat in the range of surface brightnesses around 28 mag/asec^2, preventing the determination of a unique R_{28B}. This criterion further eliminates 90 of the galaxies in our sample.

Finally, some galaxies are highly asymmetric and will be poorly described by our assumption of elliptical isophotes. As noted previously, we take the center of each galaxy to be the location of its most bound particle, which generally corresponds to the peak of the stellar density distribution, whereas the geometric center of the stellar distribution is its center of mass. We thus compute $\langle\mu_B\rangle$ around the galaxy center using first the star particles in the hemisphere directed towards the center of mass, and then for the opposite hemisphere. If the difference between these two values of $\langle\mu_B\rangle$ is larger than 1 mag/asec^2, we remove the galaxy from the sample. This removes 113 galaxies, leaving us with a final sample of 6987 galaxies.

As noted above, the *ugriz* magnitudes are computed for each stellar particle without accounting for dust obscuration. To estimate the effect of dust on the surface brightnesses of the galaxies in our sample, we used the radiative transfer code SKIRT (Baes et al. 2003, 2011; Camps & Baes 2015) as described in Appendix A. Overall, we find that including dust would not significantly affect our results, and we neglect it for the remainder of this paper.

We would like to separate the effect of the mass-to-light ratio on the surface brightness of galaxies from that of differences in their stellar mass surface density. For comparison, we compute the surface density in the form of a "fixed M/L

[1] www.sdss3.org/dr10/algorithms/sdssUBVRITransform.php

surface brightness profile", using the masses of the stellar particles and assuming they have a fixed mass-to-light ratio of $3\mathrm{M}_\odot/\mathrm{L}_\odot$ in the B band. (This is a typical M/L_B for a passive galaxy in our sample.) We designate the radius of the 28 mag/asec^2 isophote identified using fixed M/L_B as R_{28m} and the mean "surface brightness" within it as $\langle\mu_m\rangle$.

2.4 Additional galaxy and dark matter halo properties

We examine the correlation between galaxy surface brightness and a number of properties of the galaxy and its host dark matter halo. Many of these are precomputed values taken from the EAGLE catalog (McAlpine et al. 2016), but we describe the computation of several others here.

2.4.1 Galaxy kinematic morphology

Following Thob et al. (2019) and Trayford et al. (2019), who analyzed the kinematic morphology of EAGLE galaxies, we compute the orbital circularity parameter (Abadi et al. 2003) of each stellar particle:

$$\epsilon_i = j_{z,i}/j_{\mathrm{circ}}(E_i), \tag{3}$$

where $j_{z,i}$ is the specific angular momentum of the particle projected along the direction of total galaxy angular momentum, and $j_{\mathrm{circ}}(E_i)$ is the specific angular momentum of a particle on a circular orbit with the same binding energy E_i. The latter is estimated as the maximum value of $j_{z,i}$ for particles with $E < E_i$.

As a measure of the overall galaxy kinematic morphology, we take the median value of ϵ_i, which we denote $\bar{\epsilon_*}$. Unlike Thob et al. (2019), we use the values of all the stellar particles bound to the subhalo rather than only those within 30 kpc, but our values are generally in agreement with theirs. They recommend $\bar{\epsilon_*} = 0.3$ as a division between disk- and bulge-dominated galaxies, based on the division between passive and star-forming galaxies found in Correa et al. (2017).

Thob et al. (2019) used EAGLE to examine the correlation between commonly-used measures of galaxy kinematic morphology in simulations, such as the fraction of counter-rotating stars and the ratio of the rotational and dispersion velocities, V/σ. They found that these different parameters exhibit tight correlations with one another, with Spearman correlation coefficient $\rho \approx 0.98$. Thus our particular choice of $\bar{\epsilon_*}$ as a kinematic indicator should not affect our results.

We additionally compute smoothed profiles of ϵ_* as a function of projected radius, using a weighted local linear fit of the nearest 10% of points (similarly as for the surface brightness profiles in §2.3). This is done for our sample of galaxies at $z = 0$ as well as their main progenitors at $z = 0.5$, in order to examine the evolution of the kinematic distribution of the stellar particles as a function of radius.

2.4.2 Ex-situ stellar mass fraction

To quantify the impact of mergers on the galaxies in our sample, we estimate the fraction of each galaxy's stellar mass formed outside of the galaxy — the ex-situ stellar mass fraction.

Galaxies merging into a more massive galaxy are often stripped of their outer stars prior to the simulation snapshot at which the merger event is recorded. These stripped stars join the more massive galaxy prior to the merger, and thus are not recorded as part of the mass merging into the galaxy during the merger event. As a result, the mass of a merging satellite at the time of a merger can be a significant underestimate of the contribution of ex-situ stars.

We instead estimate the ex-situ mass fraction as follows. For each stellar particle in EAGLE, the time at which it formed from its parent gas particle is recorded. These timesteps have much finer spacing than the spacing of the snapshots used in our galaxy merger trees. For each stellar particle within a galaxy at $z = 0$, if in the snapshot immediately after its formation it is bound to the main progenitor of the $z = 0$ galaxy, we consider it to be part of the in-situ stellar mass. Otherwise, it contributes to the ex-situ mass fraction.

This method still somewhat underestimates the fraction of ex-situ stellar mass, because stars that form in a galaxy less than one snapshot (≤ 1.35 Gyr) before it merges into a more massive galaxy will be counted as in-situ mass. However, we find that this estimate of ex-situ mass is still larger than using the masses of non-main progenitors at the time of a merger.

2.4.3 Matched dark matter only halos

We would like to investigate whether the properties of dark matter halos influence the surface brightness of the galaxies that form within them. However, galaxies are also able to alter the properties of their host dark matter halos (e.g., Schaller et al. 2015b), leading to difficulty separating cause from effect when examining correlations between galaxy and halo properties. For this reason, we use halos from the matching dark matter only (DMO) run of the EAGLE simulation.

The DMO simulation has identical box size, resolution, and initial conditions as the reference EAGLE run. It contains $(1504)^3$ particles of dark matter, each with mass $1.15 \times 10^7 \mathrm{M}_\odot$. Each particle in the reference and DMO runs is tagged with a unique ID based on its initial conditions, such that the equivalent particles can be identified in both simulations. To find corresponding dark matter subhalos between the two simulations, we use the method described in Schaller et al. (2015b), which considers two subhalos to be "equivalent" if over half of the 50 most bound particles of each one are also bound to the other.

Because dark matter halos that become satellites are subject to stripping, which substantially alters their properties, and because some halo properties (e.g. M_{200}; see list below) are ill-defined for satellite subhalos, we examine only the properties of central galaxies/subhalos relative to their surrounding FoF halo. Of the galaxies in our sample, 4098 are hosted by central subhalos in the reference simulation, and 3826 (93.4%) of these are successfully matched to central subhalos in the DMO EAGLE run.

The dark matter halo properties we examine include:

- M_{200c}, the FoF halo mass within r_{200c}, the radius at which the mean internal density is equal to 200 times the critical density of the Universe.

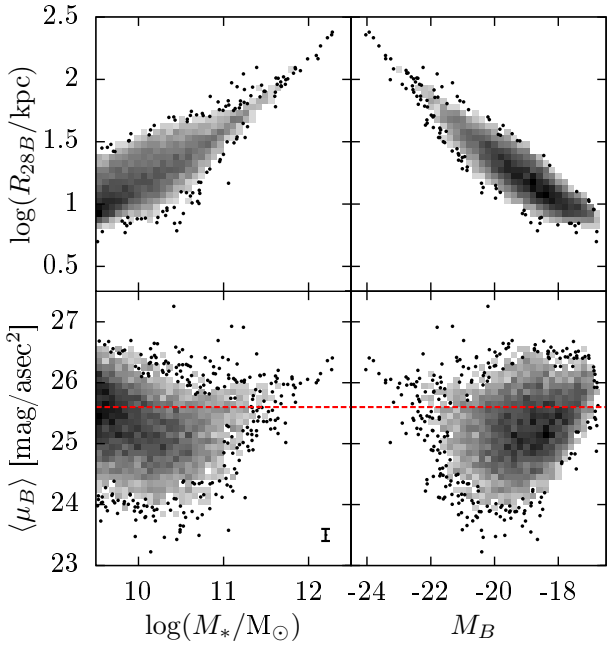

Figure 1. The distribution of radii and surface brightnesses for our sample of galaxies. The shading of each bin is proportional to the log-number of galaxies in the bin. Bins with fewer than 3 galaxies are plotted with a separate point for each galaxy. *Top left:* The circularized 28 mag/asec^2 isophotal radius in the B band, R_{28B}, as a function of galaxy stellar mass. *Top right:* R_{28B} as a function of the galaxy magnitude in the B band, M_B. *Bottom left:* The mean surface brightness within R_{28B}, $\langle\mu_B\rangle$, versus galaxy stellar mass. The error bar on the bottom right shows the median size of the error on $\langle\mu_B\rangle$, which is ±0.099 mag/asec^2. (The median error on log(R_{28B}/kpc) is ±0.012, which is smaller than the size of a plotted bin.) The red dashed line denotes $\langle\mu_B\rangle = 25.6$ mag/asec^2, which would be the value for a pure exponential disk with central surface brightness 23 mag/asec^2. *Bottom right:* $\langle\mu_B\rangle$ as a function of M_B. An upturn in $\langle\mu_B\rangle$ is visible for $M_B \lesssim -22$, or $M_* > 10^{11}$M$_\odot$. This is due to the buildup of stellar halos with $\langle\mu_B\rangle < 28$ mag/asec^2 around high-mass galaxies; see §3.1 for explanation.

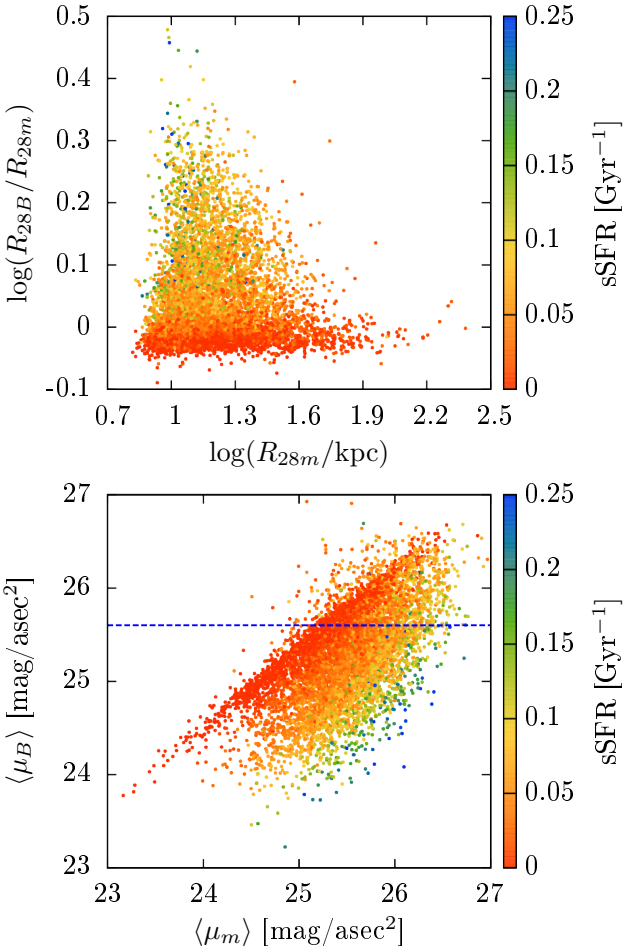

Figure 2. *Top panel:* The horizontal axis shows R_{28m}, the circularized radius of the 28 mag/asec^2 B-band isophote that each galaxy would have if $M/L_B = 3$M$_\odot$/L$_\odot$. On the vertical axis is the ratio of R_{28B} to R_{28m}; the true value of M/L_B for most galaxies is such that $R_{28B}/R_{28m} \gtrsim 1$. The color coding corresponds to the specific star formation rate (sSFR) of each galaxy, showing that galaxies with higher sSFR have larger R_{28B} at fixed R_{28m}, as expected from their lower mass-to-light ratios and consequently larger luminosities. *Bottom panel:* $\langle\mu_m\rangle$, the mean surface brightness if all galaxies had $M/L_B = 3$M$_\odot$/L$_\odot$, versus the true mean surface brightness, $\langle\mu_B\rangle$. There is a correlation between surface brightness and surface mass density, but with a substantial scatter. The colors again represent sSFR. Although a higher sSFR increases R_{28B}, there is a strong trend for galaxies with high sSFR to also be brighter within this radius at fixed mass surface density. The dashed blue line demarcates $\langle\mu_B\rangle = 25.6$ mag/asec^2, as in Figure 1. It can be seen that LSBGs selected in the B band comprise galaxies with very low mean surface density as well as those with typical surface densities but very low star formation rates.

- $V_{\rm max}/V_{200c}$, where $V_{\rm max}$ is the central subhalo maximum circular velocity, and $V_{200c} = \sqrt{GM_{200c}/r_{200c}}$. This quantity serves as a proxy for the halo concentration (Prada et al. 2012).
- the halo spin parameter of Bullock et al. (2001):

$$\lambda = \frac{J}{\sqrt{2}MrV}, \tag{4}$$

where J is the total angular momentum and M is the total mass within some radius r, and $V = \sqrt{GM/r}$. We compute the spin parameter within r_{200c} as well as $0.1r_{200c}$, in order to represent the spin of the entire and the "inner" halo, respectively.

3 RESULTS

3.1 Distribution of galaxy surface brightnesses

In Figure 1, we present the distribution of 28 mag/asec^2 isophotal radii and mean surface brightnesses for our $z = 0$ galaxy sample. The top row presents R_{28B}, the circularized (projected) radius of the elliptical isophote corresponding to 28 mag/asec^2 in the B band. The left column shows this value as a function of total galaxy stellar mass (M_*), and the right column as a function of the total galaxy B-band magnitude (M_B). Note that both the stellar mass and galaxy luminosity in Figure 1, as well as throughout this section,

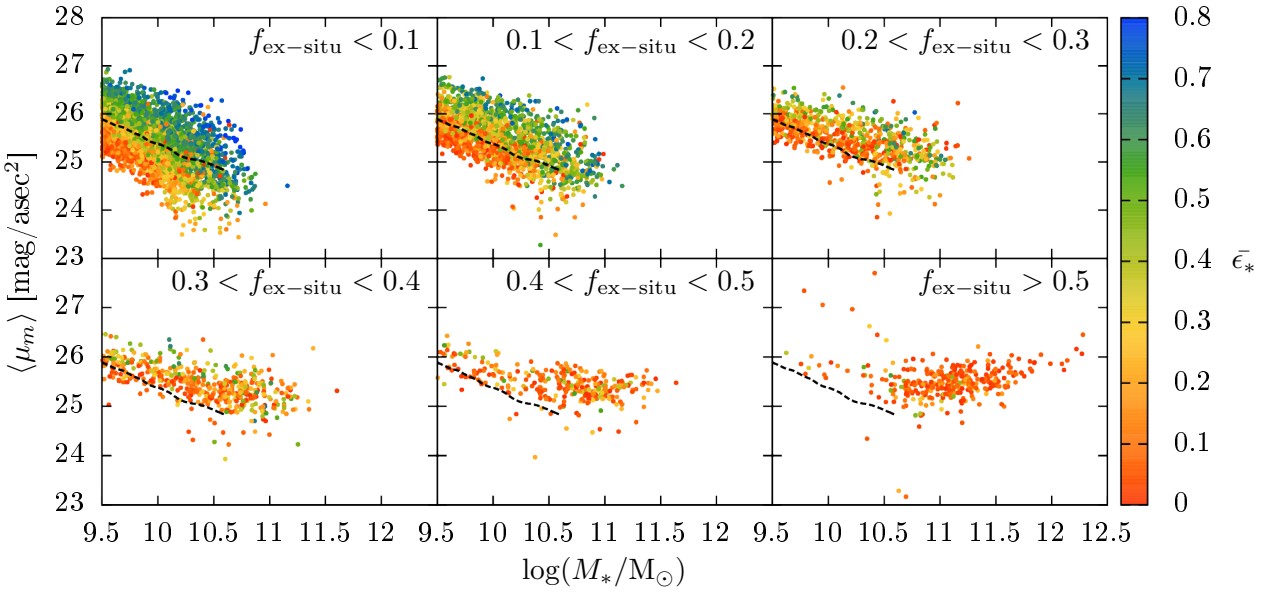

Figure 3. The relation between galaxy stellar mass and mean stellar mass surface density (expressed as $\langle \mu_m \rangle$) for bins of different ex-situ stellar mass fraction ($f_{\rm ex-situ}$): the fraction of each galaxy's stellar mass formed outside of its main progenitor branch. $f_{\rm ex-situ}$ is higher for galaxies that have gained more of their stellar mass from mergers. The dashed black line shows the median $M_* - \langle \mu_m \rangle$ relation for $f_{\rm ex-situ} < 0.1$, and is repeated in each panel to facilitate comparison. Mergers tighten the relation between M_* and $\langle \mu_m \rangle$ and lower the median surface density at fixed M_*. The latter effect is more pronounced towards higher M_*. This is a result of the buildup of the diffuse stellar halo/intracluster light component surrounding the galaxy, which lowers the *mean* surface density, as explained in §3.1. The color coding shows the median orbital circularity parameter, $\bar{\epsilon_*}$, a measure of how kinematically rotation-dominated the galaxy is (Eqn. 3). For galaxies with few mergers ($f_{\rm ex-situ} < 0.1$), $\langle \mu_m \rangle$ is essentially a function of M_* and $\bar{\epsilon_*}$. For galaxies containing an increasing fraction of stellar mass from mergers, the kinematic morphologies become more uniformly dispersion-dominated ($\bar{\epsilon_*} \approx 0$).

are the *total* mass/luminosity of *all* the star particles bound to the galaxy's subhalo. This is in contrast to most other papers using the EAGLE simulation, which measure these quantities within a 3D aperture of 30 pkpc (e.g. Schaye et al. 2015), but in doing so exclude any contribution from extended parts of the galaxy.

We see that R_{28B} has a strong positive correlation with galaxy B-band luminosity, whereas the relationship between R_{28B} and M_* is less tight, particularly at lower masses. This is due to the scatter in galaxy mass-to-light ratio in the B band at fixed stellar mass.

In the bottom panels, we show the correlation of $\langle \mu_B \rangle$ with M_* and M_B. Although $\langle \mu_B \rangle$ corresponds to the mean surface brightness rather than the central surface brightness of the galaxy disk, for the purpose of comparison we place a dashed red line at 25.6 mag/asec^2, which would be the value of $\langle \mu_B \rangle$ for an exponential surface brightness profile with central surface brightness 23 mag/asec^2. We will at times use this as an approximate division between low and high surface brightness galaxies.

R_{28B} typically encloses $\approx 95\%$ of the total galaxy light, and as a result, $\langle \mu_B \rangle$ is largely determined by the size of R_{28B} at fixed M_* or M_B. Low surface brightness galaxies are those that are more extended in their light profiles at fixed luminosity.

It can be seen that there are significantly more LSBGs at low masses and faint magnitudes. This is not surprising given that most low surface brightness galaxies in observations are faint, low-mass galaxies (e.g. Dalcanton et al. 1997a). There is, however, a noticeable upturn towards fainter $\langle \mu_B \rangle$ at the highest masses ($\gtrsim 10^{11}{\rm M}_\odot$). This results from the fact that the stars considered to belong to a galaxy in EAGLE are all those which are gravitationally bound to it. This includes their stellar halos and, for the most massive galaxies, a significant fraction of the diffuse "intracluster light" component. We will discuss this in detail later in this subsection.

The surface brightness of galaxies is, naturally, influenced by their mass-to-light ratio. In the top panel of Figure 2, we compare R_{28B} to R_{28m} computed for galaxies using a fixed mass-to-light ratio of $3{\rm M}_\odot/{\rm L}_\odot$. The color coding indicates the specific star formation rate (sSFR) of each galaxy. There is a clear trend such that galaxies with more star formation have larger 28 mag/asec^2 isophotes than would be expected from their stellar mass surface density profiles with the approximate M/L of a passive galaxy. This is due to the fact that sSFR is tightly correlated with the mass-to-light ratio in the B band, a blue band that is sensitive to the presence of young stars.

We further see the influence of the sSFR in the bottom panel of Figure 2, which shows $\langle \mu_B \rangle$ versus $\langle \mu_m \rangle$. At fixed stellar mass surface density, a higher sSFR correlates strongly with a brighter galaxy, despite the fact that it also correlates with a larger R_{28B}. It is clear from the lower panel that, for the majority of galaxies, the B-band surface brightness is essentially determined by a combination of galaxy surface density and sSFR. A dashed line is again drawn at 25.6 mag/asec^2; galaxies lying above this line include both

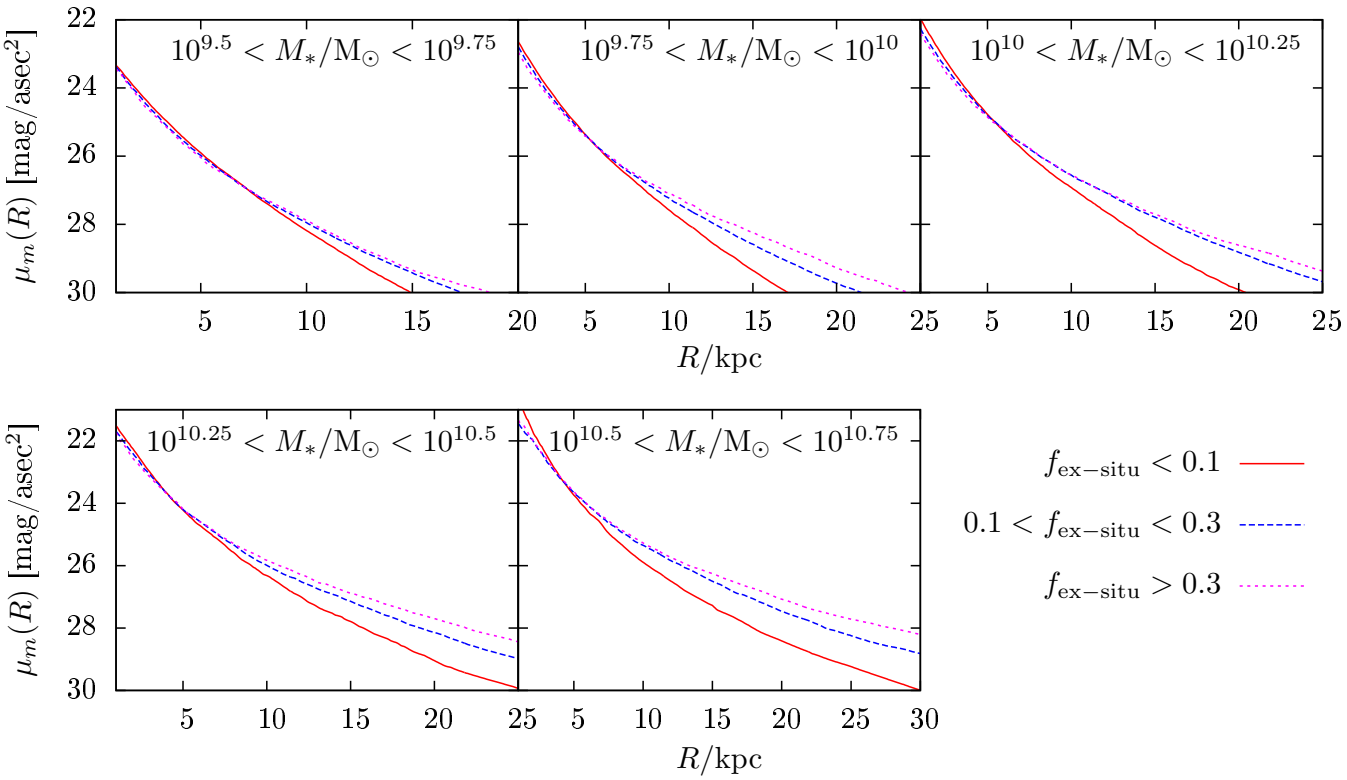

Figure 4. Median μ_m (stellar mass surface density divided by $3\mathrm{M}_\odot/\mathrm{L}_\odot$) profiles in projected radius R. Different lines in each panel are profiles for galaxies that have gained different fractions of their $z = 0$ stellar mass from mergers: red solid lines represent $f_{\mathrm{ex-situ}} < 0.1$, blue dashed lines $0.1 < f_{\mathrm{ex-situ}} < 0.3$, and magenta dotted lines $f_{\mathrm{ex-situ}} > 0.3$. Panels show bins of galaxy stellar mass. In each mass bin, the subsets of galaxies with different $f_{\mathrm{ex-situ}}$ have been selected to have the same distribution in $\bar{\epsilon_*}$, such that the differences between them are not the result of different mean kinematic morphology. It can be seen that mergers cause a diffuse stellar halo to develop in the outer parts of galaxies in all mass bins. The surface density at which the profiles diverge is larger at higher masses.

galaxies with very low surface densities and galaxies with more typical surface densities but very low sSFR.

In EAGLE, the star formation rates of galaxies have been found to vary on both long and short timescales. Matthee & Schaye (2019) found that the long-timescale variation of the star formation rate relates to the concentration of the galaxy's host dark matter halo, which correlates with the cosmic time at which the galaxy forms the majority of its stars (Matthee et al. 2017). However, the authors also noted that there was significant short-timescale variation in the SFR of galaxies. Given the correlation between sSFR and surface brightness seen in Figure 2, the surface brightnesses of galaxies likely also exhibit some short-timescale variation.

Having seen the correlation between $\langle\mu_B\rangle$ and $\langle\mu_m\rangle$, we now turn back to the influence of stellar halos/ICL. In Figure 3, we plot the galaxy stellar mass versus $\langle\mu_m\rangle$, in bins of different ex-situ stellar mass fraction. Galaxies with $f_{\mathrm{ex-situ}} < 0.1$ have had little influence from mergers. From left to right and top to bottom, galaxies with an increasing stellar mass contribution from mergers are shown. The color coding shows the median orbital circularity parameter, $\bar{\epsilon_*}$, a measure of how kinematically rotation-dominated the galaxy is (see Eqn. 3 and §2.4.1). For galaxies with little contribution from mergers, the stellar mass surface density at fixed M_* is largely a function of the kinematic morphology, with more disk-dominated galaxies being less dense. As $f_{\mathrm{ex-situ}}$ increases, a larger fraction of galaxies are dispersion-dominated, and the correlation between $\langle\mu_m\rangle$ and kinematic morphology gradually disappears. At fixed stellar mass, the distribution of $\langle\mu_m\rangle$ becomes tighter, and its mean value becomes larger (lower density). The latter effect is increasingly pronounced for larger stellar masses.

Figure 4 reveals the reason for some of these trends with ex-situ mass fraction. Here we plot the median $\mu_m(R)$ profiles for galaxies in different stellar mass bins and with different ex-situ stellar mass fractions. In each mass bin, we subsample the galaxies with different $f_{\mathrm{ex-situ}}$ such that they have the same distribution in $\bar{\epsilon_*}$; thus the differences in their stellar mass density profiles are not simply the result of different mean kinematic morphology. At small radii, the μ_m profiles of galaxies with different ex-situ mass fractions are similar. However, at all masses, galaxies that have experienced more mergers have more extended low-density (faint) outer parts. This faint component corresponds to the stellar halo, or, for the most massive galaxies, the "intracluster light". Because the *fraction* of mass contained in this component is largely determined by $f_{\mathrm{ex-situ}}$, the stellar halo dominates the mass surface density profile beginning at higher surface densities with increasing stellar mass, as can be seen by comparing the panels of Figure 4. As a result, the value of R_{28m} is increased more for higher-mass galaxies, and the mean surface density within R_{28m} is cor-

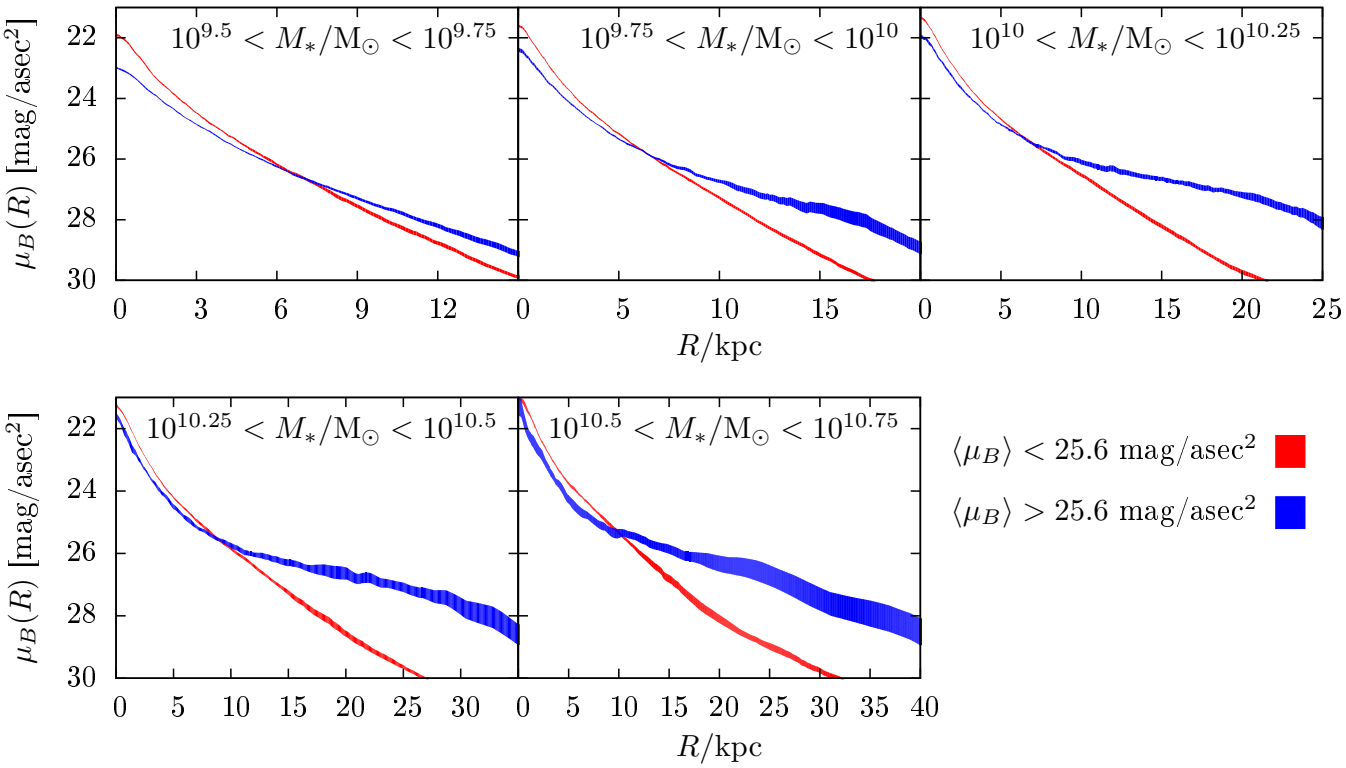

Figure 5. Median surface brightness profiles for galaxies with little mass gain from mergers ($f_{\mathrm{ex-situ}} < 0.1$), in different stellar mass (M_*) bins. The red curves are the median profiles for galaxies with $\langle\mu_B\rangle < 25.6$ mag/asec^2 (approximately, "high surface brightness galaxies"), and the blue ones are the profiles of those with $\langle\mu_B\rangle > 25.6$ mag/asec^2 ("low surface brightness galaxies"). The thickness of the curves represents the one-sigma errors on the median. LSBGs in all mass bins have a faint outer disk component with a shallow surface brightness profile.

respondingly decreased. This is responsible for the trend in Figure 3 whereby mergers increase the mean value of $\langle\mu_m\rangle$ more for galaxies with higher stellar masses. It is similarly responsible for the upturn in $\langle\mu_B\rangle$ seen at high masses in Figure 1. We note that the magnitude of this effect is sensitive to the particular choice of isophote within which the mean surface brightness is measured, as this determines the galaxy mass at which the stellar halo begins to influence the location of the isophote.

In Figure 3 and Figure 4, galaxy mergers are shown to have two typical effects: they cause galaxies to become more kinematically spheroid-dominated, and they build up a diffuse stellar halo in the outskirts of the galaxy. Nevertheless, a minority of rotation-dominated galaxies ($\bar{\epsilon}_* > 0.3$) are visible even in the panels with high ex-situ mass fractions in Figure 3. We will demonstrate in §3.5 that in a minority of cases, mergers can in fact increase the spin of galaxies as well as contribute to a faint outer *disk* rather than a spheroidal halo. However, we will first focus on the formation of LSBGs with low ex-situ mass fractions, as it is clear from Figure 1 that the majority of LSBGs are low-mass galaxies, which tend to have relatively quiescent merger histories (Figure 3).

3.2 Surface brightnesses of galaxies with low ex-situ mass fractions

We now investigate the surface brightnesses of galaxies that have undergone a predominantly secular evolution in recent times. We focus specifically on galaxies with an ex-situ stellar mass fraction less than 0.1. This subsample contains galaxies with stellar masses $M_* \lesssim 10^{10.75}\mathrm{M}_\odot$, and comprises $\approx 60\%$ of galaxies with these masses.

While mergers clearly alter the properties of the galaxy population, the magnitude of the effect depends on how much stellar mass they contribute, as can be seen from the sequence of panels in Figure 3. Although the following three subsections focus on a subsample of galaxies with very little influence from mergers, our qualitative conclusions would be unchanged if we instead considered the all galaxies with $f_{\mathrm{ex-situ}} < 0.2$, which includes 81% of all galaxies with $M_* < 10^{10.75}\mathrm{M}_\odot$, although the scatter in the correlations we identify would be larger. We therefore note that the LSBG properties and formation scenario identified in the following subsections likely apply to the considerable majority of low-mass LSBGs, which also dominate the overall LSBG population for $M_* > 10^{9.5}\mathrm{M}_\odot$.

In Figure 5, we show the median surface brightness profiles of galaxies with $f_{\mathrm{ex-situ}} < 0.1$ split into different bins of stellar mass. Each bin is further split into HSBGs ($\langle\mu_B\rangle < 25.6$) and LSBGs ($\langle\mu_B\rangle > 25.6$). Note that the

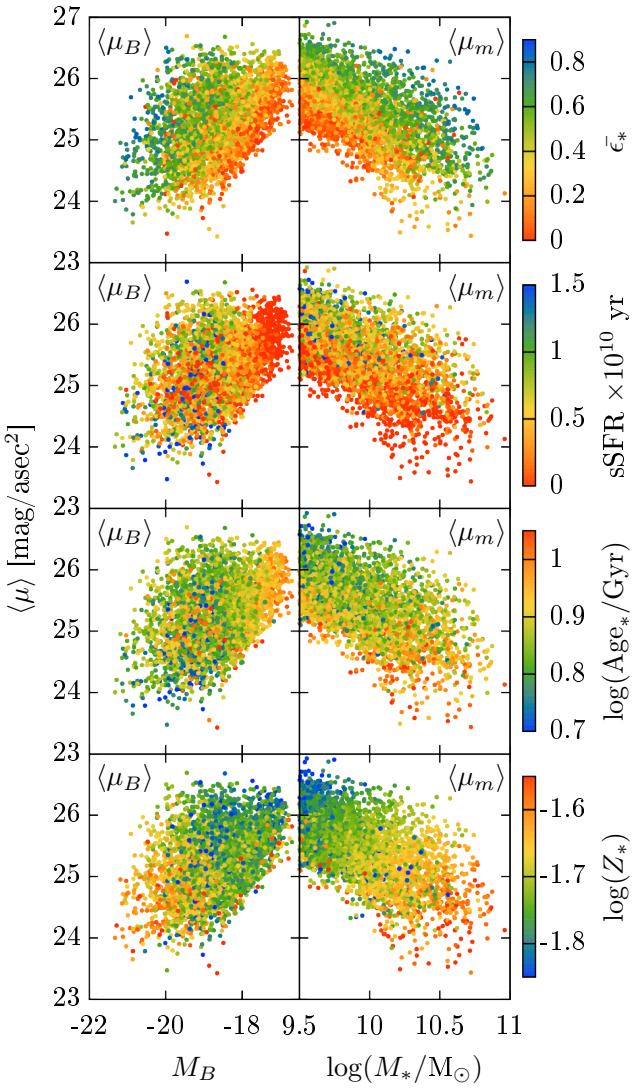

Figure 6. For galaxies with $f_{\rm ex-situ} < 0.1$, the correlation of various galaxy properties with M_B and $\langle\mu_B\rangle$ in the left column, and with M_* and $\langle\mu_m\rangle$ in the right column. The color coding is as follows. *Top row:* The median orbital circularity parameter, $\bar{\epsilon_*}$, a measure of the kinematic morphology of each galaxy. The right-hand panel is the same as the top left-hand panel of Figure 3. The tight relation between kinematic morphology and stellar mass surface density at fixed stellar mass produces a similarly tight relation between M_B, $\langle\mu_B\rangle$, and $\bar{\epsilon_*}$. *Second row:* Specific star formation rate (sSFR). Lower surface density correlates with higher sSFR (right panel). However, surface brightness in the B band is positively correlated with a high sSFR (see Figure 2), so there is little correlation between sSFR and $\langle\mu_B\rangle$ (left panel). The increase in $\langle\mu_B\rangle$ at low luminosity is a selection effect due to the fact that we select galaxies with a fixed M_* cut, so the least luminous galaxies are those with low sSFR (high M/L_B). *Third row:* The initial-mass-weighted mean stellar age of each galaxy. Trends are similar to those with sSFR. *Bottom row:* The stellar metallicity (metal mass fraction) of each galaxy, Z_*. There is a tight relation between $\langle\mu_m\rangle$ and stellar metallicity at fixed M_* seen in the right panel. This correlation persists, albeit with more scatter, between Z_* and $\langle\mu_B\rangle$ at fixed M_B, such that lower surface brightness galaxies are more metal-poor.

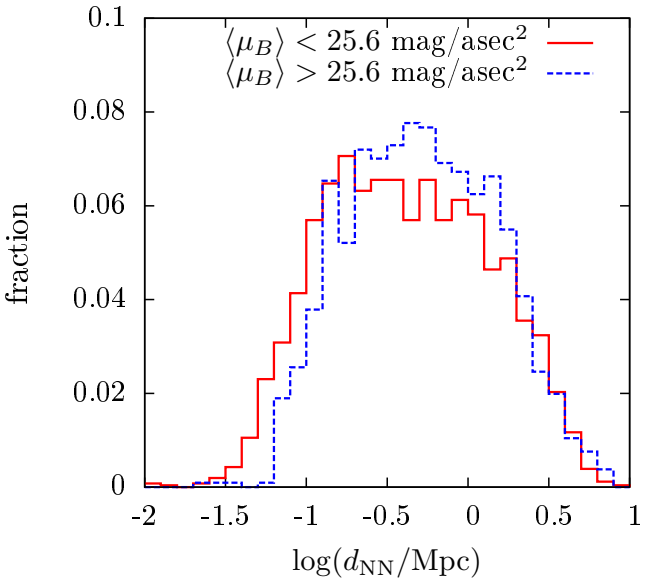

Figure 7. For galaxies with $f_{\rm ex-situ} < 0.1$, the normalized distribution of log-distance to the nearest neighbor galaxy, for LSBGs ($\langle\mu_B\rangle > 25.6$ mag/asec^2; blue dashed line) and HSBGs ($\langle\mu_B\rangle < 25.6$ mag/asec^2; red solid line). "Neighbors" are defined to be any galaxy with $M_* > 10^9 M_\odot$. LSBGs tend to be farther from their nearest neighbor than HSBGs.

number of HSBGs and LSBGs varies depending on the bin. For the lowest mass galaxies, with $10^{9.5} < M_*/M_\odot < 10^{9.75}$, the median surface brightness profile of LSBGs is shallower at all radii than that of HSBGs. At higher masses, the central regions of the LSBGs have similar profile slopes as HSBGs, indicating the presence of a nucleus. In EAGLE, it has been found that central spheroids can grow within galaxies even in the absence of mergers, due to the secular transformation of disks into spheroids (Trayford et al. 2019). Nevertheless, in all mass bins there is a clear faint disk component present in the LSBG subsample.

We now examine the correlations between galaxy surface brightness, galaxy surface density, and various galaxy properties. Given that surface brightness is largely a function of surface density and star formation rate (Figure 2), we expect many of the galaxy properties correlated with galaxy surface density to also correlate with surface brightness.

In Figure 6, we show in the left column of panels the galaxy B-band magnitude M_B versus $\langle\mu_B\rangle$. In the right column we show the galaxy stellar mass M_* versus $\langle\mu_m\rangle$. In the top row, the colors show the median orbital circularity parameter, $\bar{\epsilon_*}$, as in Figure 3. The correlation between $\bar{\epsilon_*}$ and surface density also extends to surface brightness, such that low surface brightness galaxies are more rotation dominated. This agrees with observations of "classical" LSBGs, which have disky morphologies, unlike UDGs, which tend to be dispersion dominated.

In the second row of panels in Figure 6, the color coding represents the specific star formation rate. In the right panel, we see that galaxies with lower surface densities have higher sSFR at fixed stellar mass. This is unsurprising given the tight correlation between surface density and kinematic morphology, as rotation-dominated galaxies

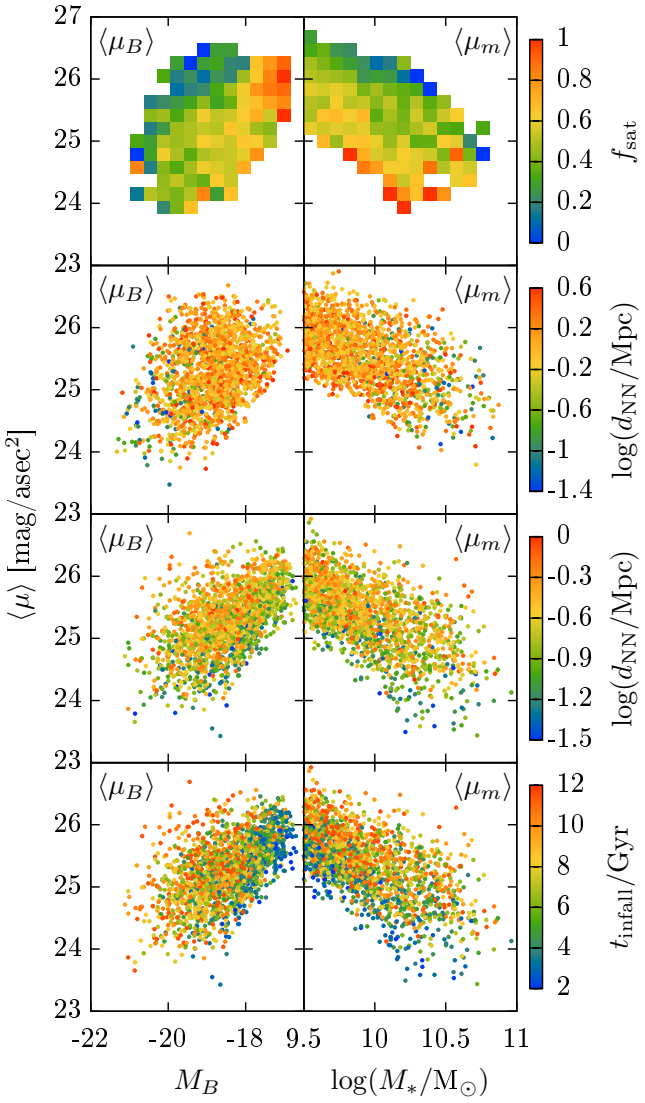

Figure 8. Like Figure 6, but now color-coded by properties related to the spatial distribution of galaxies. *Top row:* $f_{\rm sat}$, the fraction of galaxies in each bin that are satellites. Only bins containing ≥ 5 galaxies are shown. Galaxies with lower surface brightness are less likely to be satellites. *Second row:* The distance to the nearest neighbor galaxy ($d_{\rm NN}$), for central galaxies only. Here "neighbors" are defined as any galaxy with $M_* > 10^9 {\rm M}_\odot$. Note that many centrals have no satellites above this mass cut — i.e., their nearest neighbor is a central. No significant trend exists between surface brightness and $d_{\rm NN}$ for centrals. *Third row:* $d_{\rm NN}$ for galaxies in our sample that are satellites. Satellites with lower surface brightnesses tend to be farther from their nearest neighbor. *Bottom row:* For satellites, the cosmic time at which the galaxy became a satellite, $t_{\rm infall}$. Satellites with lower surface brightnesses fell into their hosts more recently.

in EAGLE are known to have higher star formation rates (Correa et al. 2017). However, since a higher sSFR also increases the brightness of the galaxy, the same trend does not persist in the left panel of the second row, where sSFR is shown as a function of surface brightness and magnitude. For the least luminous galaxies ($M_B > -18$), the sSFR is uniformly low, but this is a selection effect due to the fact that our sample is based on a fixed stellar mass cut, so the least luminous galaxies are those with the lowest star formation rates. For more luminous galaxies, there is clearly a large scatter in the sSFR of galaxies at fixed $\langle\mu_B\rangle$ and M_B.

For $M_B < -18$, we find that galaxies with $\langle\mu_B\rangle < 25.6$ (HSBGs) have a median sSFR of 4.3×10^{-11} yr^{-1} while those with $\langle\mu_B\rangle > 25.6$ (LSBGs) have a median value of 5.9×10^{-11} yr^{-1}. Although LSBGs have been recorded in some papers as having low star formation rates (van der Hulst et al. 1993; van den Hoek et al. 2000), others find that their sSFRs are not significantly different from those of HSBGs (Galaz et al. 2011; Du et al. 2019), which is similar to what we find in EAGLE.

The third row of Figure 6 shows the mean stellar population age of each galaxy, computed as the mean age of the star particles weighted by their initial (i.e. prior to mass loss) particle mass. In the right panel, the trend is similar to that seen for sSFR, such that star-forming galaxies are also younger. Since the subsample of galaxies shown in this figure is experiencing a predominantly secular evolution, galaxies that are younger tend to have higher sSFR because they undergo their peak of star formation later in cosmic time (Matthee & Schaye 2019). However, in the left panel we again see a lack of correlation between surface brightness and mean stellar age. We find a median stellar age of 7.31 Gyr for galaxies with $\langle\mu_B\rangle < 25.6$ and 7.25 Gyr for those with $\langle\mu_B\rangle > 25.6$ — a negligible difference.

The bottom panels of Figure 6 show the correlation of $\langle\mu_B\rangle$ and $\langle\mu_m\rangle$ with stellar metallicity (total metal mass fraction) of each galaxy. The mass-metallicity relation (e.g. Tremonti et al. 2004) is visible on average, but at fixed stellar mass, there is a significant trend between metallicity and mean stellar mass surface density. A correlation between metallicity and local stellar density within galaxies has been noted previously in EAGLE (Trayford & Schaye 2019) as well as in observations of real galaxies (Moran et al. 2012; Sánchez et al. 2013). This correlation translates to a somewhat weaker trend with surface brightness in which lower surface brightness galaxies are more metal-poor, in agreement with observations of LSBGs (McGaugh 1994; de Blok & van der Hulst 1998; Burkholder et al. 2001).

We now examine the spatial distribution of galaxies as a function of surface brightness. In Figure 7, we show the distribution of nearest-neighbor distances for galaxies split into LSBGs and HSBGs. Here "neighbors" are defined as any galaxy with $M_* > 10^9 {\rm M}_\odot$, but we see qualitatively similar trends if we use a lower stellar mass limit, or define "neighbors" as galaxies with stellar masses above some fraction of the mass of the galaxy being considered. LSBGs are less likely than HSBGs to be at close distances to their nearest neighbor, consistent with observations of LSBGs (Bothun et al. 1993; Rosenbaum & Bomans 2004; Galaz et al. 2011).

We further examine this difference in Figure 8, which is the same as Figure 6 but with color coding representing spatial properties of galaxies. The top row of panels show the fraction of galaxies that are satellites in bins containing at least five galaxies each. Recall that in EAGLE, every FoF halo has a central galaxy that contains the most bound particle, and all other galaxies are "satellites". We see that for both surface density and surface brightness, low/faint values correlate with a lower fraction of objects that are satellites. It is worth noting that the increase in satellite fraction for

low-luminosity galaxies is again the effect of selecting a sample based on a stellar mass cut, as high M/L_B galaxies tend to be quenched satellites.

In the second and third rows, we show the distance to the nearest neighbor for galaxies split into centrals (second row) and satellites (third row). For central galaxies, there is no significant correlation between the distance to the nearest neighbor and the surface density or surface brightness at fixed stellar mass or magnitude. (We note that many centrals in fact have zero satellites with $M_* > 10^9 \mathrm{M}_\odot$, but we see the same lack of correlation if using a lower mass limit for "neighbors".)

However, for satellite galaxies, shown in the third row, there is a clear correlation between surface brightness and distance to the nearest neighbor, such that galaxies with lower surface brightness are farther from their nearest neighbor. Furthermore, in the bottom row of Figure 8, we show for satellite galaxies the time at which they became a satellite (estimated as the cosmic time of the last snapshot during which they were not a satellite). Low surface brightness satellites are those that fell into their host recently, whereas high surface brightness satellites have been satellites for a long time.

The combination of factors above suggests that LSBGs and HSBGs in EAGLE do not form (as central galaxies) in substantially different environments, but rather that encounters with other massive galaxies tend to disrupt LSBGs. This is why LSBGs are less likely to be satellites, and when they are satellites, they are not close-in satellites that fell into their host halo long ago.

3.3 Dark matter halo properties of LSBGs with low ex-situ mass fractions

Having seen in §3.2 that LSBGs and HSBGs form in similar environments, we now present the correlation of galaxy surface brightness with various host dark matter halo properties. While the properties of dark matter halos are thought to determine many of the properties of the galaxies that form within them, baryonic physics can change the distribution of dark matter, especially on galactic scales, making it challenging to disentangle the influence of halos on galaxies from that of galaxies on halos. As described in §2.4.3, we avoid this problem by examining the properties of "matched" dark matter halos from a dark matter only (DMO) run of EAGLE with identical initial conditions to the Ref-L0100N1504 reference run. Thus the dark matter halo properties presented here have been run. Thus the dark matter halo properties presented here have been unaffected by baryonic physics. For the reasons given in §2.4.3, as well as the fact that LSBGs seem to be destroyed by satellite stripping processes, we present galaxy-halo correlations only for central galaxies/subhalos.

While EAGLE produces, on average, realistic galaxy rotation curves (Schaller et al. 2015b), it has been noted that the scatter in the rotation curves for low-mass galaxies is less than what is found in observations (Oman et al. 2015). LSBGs in particular are typically observed to have very slowly rising rotation curves (Swaters et al. 2000; Lelli et al. 2016). Factors that have been put forth as possibly contributing to this discrepancy include the lack of halo core formation in EAGLE and similar simulations (Katz et al. 2017; Santos-Santos et al. 2018; see however Benítez-Llambay et al. 2019), as well as misestimation of some observed dwarf galaxy rotation curves due to non-circular gas motions (Oman et al. 2019). The fact that the source of this disagreement has not been found highlights our incomplete understanding of the relationship between low-mass galaxies and their dark matter halos. We therefore caution that it is not certain that EAGLE forms such galaxies in the correct dark matter halos.

In Figure 9, we present the correlation of several halo properties with the stellar mass of the central galaxy. These centrals are split into LSBGs and HSBGs using a cut of $\langle \mu_B \rangle = 25.6$ mag/asec^2. Additionally, the same correlations are shown for "low density" and "high density" galaxies, using the same threshold in $\langle \mu_m \rangle$. The curves are computed using a boxcar smoothing of ± 0.1 dex in M_*. While the results presented in this figure use the matched DMO halo properties, we note that similar results are found using the host halo properties from the reference simulation.

In the top left panel, we show the ratio of the halo mass, M_{200c}, to the stellar mass, M_*. It can be seen that LSBGs and HSBGs of the same stellar mass form in dark matter halos of similar masses. In the lower left panel, we show the ratio $V_{\mathrm{max}}/V_{200c}$, a proxy for the halo concentration (Prada et al. 2012). LSBGs appear to inhabit slightly more concentrated halos than HSBGs, but interestingly, this trend seems to be reversed (at $M_* \lesssim 10^{10}\mathrm{M}_\odot$) or non-existent (at $M_* \gtrsim 10^{10}\mathrm{M}_\odot$) for galaxies split by their mean surface density rather than their mean surface brightness. This is likely due to the fact that halo concentration, which correlates strongly with the assembly time of the halo (Wechsler et al. 2002), has also been found to correlate with the mean stellar age of the central galaxy in EAGLE (Matthee et al. 2017) and its star formation rate (Matthee & Schaye 2019). We have seen that galaxies with faint mean surface brightness tend to have older ages and lower sSFRs relative to galaxies with low surface mass density (Figure 3 and Figure 6). Since the central galaxies of halos with larger concentrations are older, we would expect LSBGs to reside in halos with higher concentration than galaxies selected based on low stellar mass surface density.

The top right panel of Figure 9 shows the spin parameter, λ, of the dark matter halo within r_{200c} as a function of central galaxy stellar mass. Here there is a noticeable division between LSBGs and HSBGs, such that the former are hosted by halos with larger spins. The same is true for galaxies with low and high stellar mass surface density. However, we note that while the difference in the median halo spin between the two populations is statistically significant, it is much smaller than the scatter in the halo spin within the two groups. We will comment more on the evolutionary implications of this in the discussion subsection below.

Finally, in the bottom right panel of Figure 9 we show the ratio of total baryonic mass in the central subhalo — including stars and both hot and cold gas — to the halo mass, M_{200c}. LSBGs have higher baryonic masses than HSBGs, and given that it is clear from the top left panel that they do not have substantially higher halo masses at fixed stellar mass, this implies that they have higher gas masses. This is true despite the fact that LSBGs do not have significantly higher specific star formation rates than HSBGs (Figure 5),

meaning that much of their excess gas mass is in the form of non-star-forming gas.

3.4 The formation of low-mass LSBGs

Based on the correlations between surface brightness and galaxy and halo properties presented above, a coherent picture emerges of the formation of low surface brightness galaxies with little mass contribution from mergers, which are the dominant type of LSBG at stellar masses between $10^{9.5}$ and $10^{10.5}\mathrm{M}_\odot$.

First, it is clear from Figure 3 and Figure 6 that LSBGs at low stellar masses are to a significant extent the high angular momentum tail of the galaxy distribution. In blue optical bands such as the B band, there is some scatter in the surface brightness at fixed galaxy kinematic morphology that results from scatter in the mass-to-light ratio, which is highly correlated with the specific star formation rate of the galaxy and the mean age of its stellar population. Galaxies that are more rotation-dominated generally have higher sSFRs, but this increases their surface brightness, and thus galaxies selected to have low surface brightness have some scatter in their kinematic morphology, and a significant amount in their sSFR and mean stellar age.

The formation of spheroid- and disk-dominated galaxies in EAGLE has already been examined by a number of authors. Zavala et al. (2016) found that most stars in disk-dominated galaxies are formed after the turnaround time of the galaxy's assembling host dark matter halo. These stars are formed from a gas reservoir whose angular momentum is set by the spin of the host halo at late times, resulting in a correlation between the spin of the stellar component and that of the host halo. Conversely, the majority of stars in spheroidal galaxies are formed prior to turnaround, and the final angular momentum of the galaxy is mostly correlated with that of the inner regions of the dark matter halo, rather than the entire halo. Zavala et al. (2016) attribute the latter to mergers subsequent to turnaround, which lead to a loss of angular momentum for both the stellar component and inner halo.

Clauwens et al. (2018) also examined the formation of the spheroid and disk components of galaxies in EAGLE, finding a "three-phase" evolution set by a galaxy's growth progression through different stellar masses. In contrast to Zavala et al. (2016), Clauwens et al. (2018) find that for $M_* \lesssim 10^{10}\mathrm{M}_\odot$, galaxies grow as kinematic spheroids via a combination of in-situ star formation and "tiny" mergers of mass ratio less than 1:10. Higher-mass galaxies begin to develop disks around their spheroidal component through in-situ star formation, and at the highest masses ($M_* \gtrsim 10^{10.5}\mathrm{M}_\odot$), enhancement of the dispersion-dominated component recommences, but only via mergers. This agrees with our Figure 3, where it can be seen that spheroid-dominated galaxies with low ex-situ mass fractions are nearly absent for $M_* > 10^{10}\mathrm{M}_\odot$.

Our results are consistent with the evolutionary scenarios described above. The galaxies with the lowest surface mass density are those that are the most disk dominated. These galaxies are young, having formed their stars more recently on average (Figure 6), and they inhabit halos with higher spins (Figure 9), in agreement with Zavala et al. (2016). However, low surface brightness is anticorrelated with young stellar population ages and high star formation rates (Figure 2 and Figure 6), so there is no remaining correlation between galaxy surface brightness and stellar population age. Nevertheless, galaxies with the highest angular momentum are still those in the highest-spin halos, and thus a significant correlation remains between host halo spin and galaxy surface brightness.

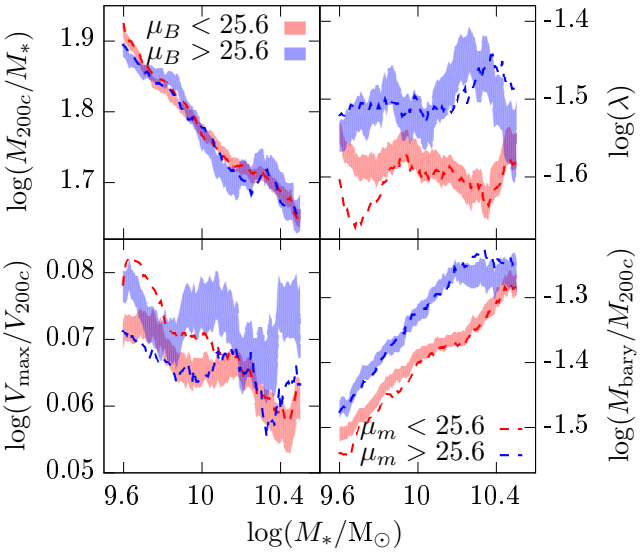

Figure 9. The mean value of various dark matter halo properties as a function of central galaxy stellar mass. All halo properties are taken from the dark matter only variant of the EAGLE simulation, and are thus unaffected by baryonic physics (see §2.4.3 for details). The blue and red bands represent the error around the mean for LSBGs ($\langle\mu_B\rangle > 25.6$ mag/asec^2) and HSBGs ($\langle\mu_B\rangle < 25.6$ mag/asec^2), respectively. Additionally, each panel shows, as dashed lines with the same color coding, the mean value for galaxies with low stellar mass surface density ($\langle\mu_m\rangle > 25.6$ mag/asec^2) and high stellar mass surface density ($\langle\mu_m\rangle < 25.6$ mag/asec^2). *Top left:* The mean ratio of dark matter halo mass (M_{200c}) to central galaxy stellar mass. LSBGs and HSBGs have essentially the same stellar-halo mass relation. *Bottom left:* The mean value of $V_{\rm max}/V_{200c}$, a proxy for the halo concentration. LSBGs have slightly more concentrated halos than HSBGs; however, the halo concentration of low *density* galaxies is slightly *lower* than that of high density galaxies. This is because concentration correlates with galaxy age (see text). *Top right:* The mean halo spin parameter. LSBGs inhabit higher spin halos than HSBGs. *Bottom right:* The ratio of total baryonic mass (hot gas, cold gas, and stars) in the central subhalo to halo mass M_{200c}. LSBGs have a higher baryon fraction and are more gas rich than HSBGs.

In addition to the properties presented in Figure 9, we also computed the correlation of the surface brightness with the spin of the "inner halo", defined as the particles within $0.1r_{200c}$. While we did find a correlation, it was lower than that between the surface brightness and the spin of the entire halo. This is in agreement with the conclusions of Zavala et al. (2016), which imply that low-mass galaxies with few mergers should have angular momentum that is better correlated with the large-scale spin of the halo.

Our conclusions agree partially with the recent work of Di Cintio et al. (2019), who studied a sample of 12 galax-

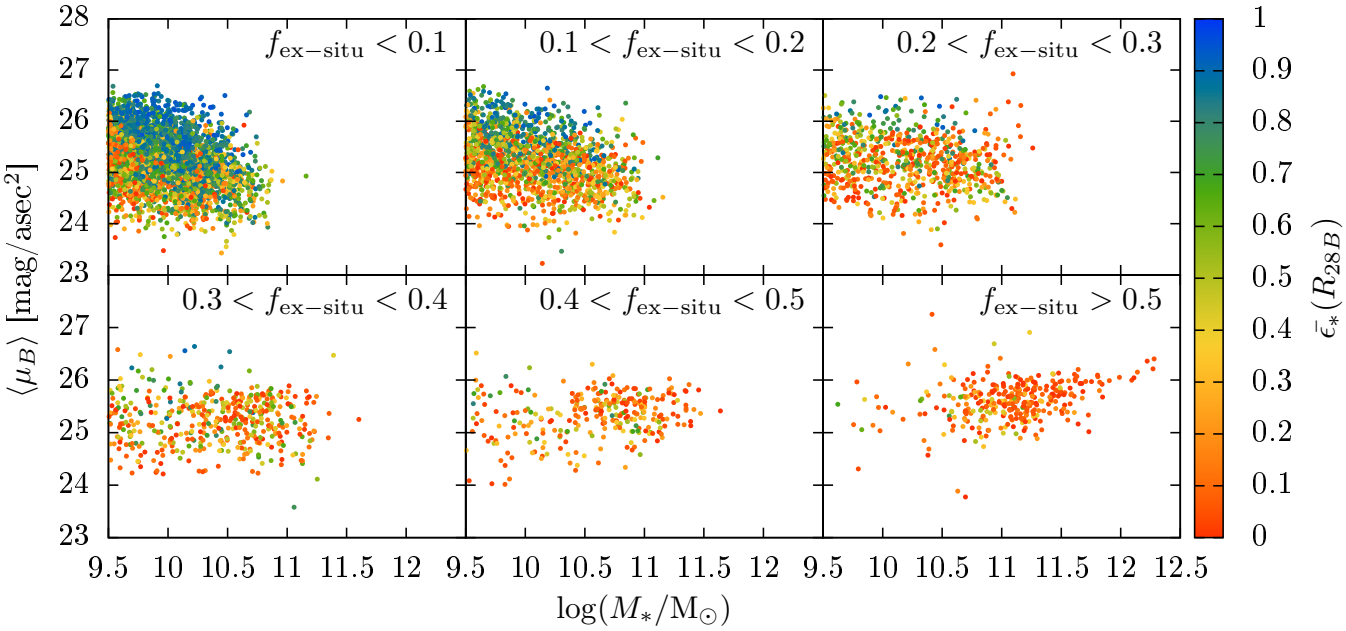

Figure 10. Like Figure 3, but showing the stellar mass M_* versus $\langle \mu_B \rangle$, with color coding representing the local value of the orbital circularity, $\bar{\epsilon}_*$, at R_{28B}. $\bar{\epsilon}_*(R_{28B})$ typically correlates well with $\bar{\epsilon}_*$ of the entire galaxy: the local value at R_{28B} is ≈ 0.5 for disk-dominated galaxies. It is notable that some galaxies with high ex-situ stellar mass fractions have significant kinematic rotation even at R_{28B}, in their faint outer parts.

ies with $10^{9.5} < M_*/{\rm M}_\odot < 10^{10}$, including both LSBGs and HSBGs, in the NIHAO suite of hydrodynamical zoom-in simulations (Wang et al. 2015). The authors found that LSBGs form in halos with higher spins, and lack a significant correlation with any other halo parameters. However, they also found that this is primarily the result of galaxy mergers, with higher spin galaxies and halos having had more aligned rather than misaligned mergers. Here we find that galaxies that have had very little merger activity have a significant range of kinematic morphologies and surface brightnesses.

3.5 The effect of mergers on surface brightness

In the previous subsection, we described how low surface brightness galaxies can form through (nearly) secular evolution, via growth of their stellar disks at late times from a reservoir of gas co-rotating with a high-spin host halo. However, the highest-mass galaxies in EAGLE, with stellar masses comparable to the estimated value for Malin 1 ($\approx 10^{11}{\rm M}_\odot$; Boissier et al. 2016), have all undergone significant mass growth from mergers (Figure 3).

From Figure 3 and Figure 4, it is clear that mergers typically make galaxies more kinematically dispersion dominated, and also build up a faint outer stellar halo. However, in Figure 3 it is also possible to see a few massive galaxies with significant mass growth from mergers that nevertheless have $\bar{\epsilon}_* > 0.3$, implying they are disk-like.

The mass of galaxies is dominated by their inner regions, so a high median orbital circularity for the whole galaxy does not necessarily imply that these massive galaxies are kinematically disk-like in their faint outer regions, which may consist of a dispersion-dominated stellar halo. We examine this in Figure 10, which is very similar to Figure 3, but shows $\langle \mu_B \rangle$ rather than $\langle \mu_m \rangle$ as a function of stellar mass, and the color coding indicates the *local* $\bar{\epsilon}_*$ at R_{28B} for each galaxy, computed from the smoothed curve of ϵ_* as a function of projected radius. For the full galaxy sample, $\bar{\epsilon}_*(R_{28B})$ correlates strongly with $\bar{\epsilon}_*$ such that $\bar{\epsilon}_* = 0.3$ corresponds to $\bar{\epsilon}_*(R_{28B}) \approx 0.5$. We therefore use this value of $\bar{\epsilon}_*(R_{28B})$ as an approximate division between galaxies that have a significant disk component at R_{28B} and those that are spheroid-dominated. We see in the lower panels of Figure 10 that some galaxies with substantial mass from mergers are indeed rotation-dominated even in their outskirts.

Unlike Figure 3, Figure 10 shows $\langle \mu_B \rangle$, and thus the correlation with kinematic morphology is weaker due to scatter in M/L resulting from different values of the star formation rate. Additionally, we see that for massive galaxies, which have high ex-situ mass fractions, there is little difference between the trends in $\langle \mu_B \rangle$ in Figure 10 and those in $\langle \mu_m \rangle$ in Figure 3. This is because high-mass galaxies tend to have uniformly low sSFR and therefore little scatter in M/L values. There remains some correlation between sSFR and $\bar{\epsilon}_*$ even for massive galaxies with high ex-situ fractions, but overall the sSFR induces significantly less scatter in $\langle \mu_B \rangle$ than at low mass. For the remainder of this subsection, we will focus on the role of mergers in creating large, low-density disks, and ignore the scatter in $\langle \mu_B \rangle$ due to variable M/L.

To select the most extended galaxies whose faint outer regions are disk-like rather than a dispersion-dominated stellar halo, we select all the galaxies that have $\bar{\epsilon}_*(R_{28B}) > 0.5$ and examine the ones with largest R_{28B}. On visual inspection, the largest such galaxy turns out not to be a disk galaxy but a ring galaxy. (Ring galaxies in EAGLE were studied in Elagali et al. 2018.) We thus exclude it from consideration. For the four next largest galaxies, we show mock face-on

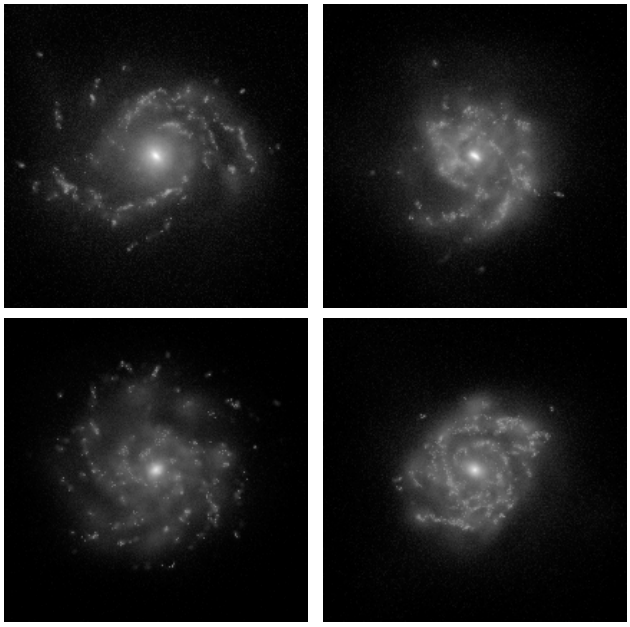

Figure 11. Synthetic B-band face-on images (including dust) of the four galaxies possessing an outer disk ($\bar{\epsilon_*}(R_{28B}) > 0.5$) having the largest values of R_{28B} in our sample. Images were created using the radiative transfer code SKIRT (see Appendix A), and are 200 pkpc per side with pixel size 0.94 pkpc and logarithmic flux scaling. *Top Left:* GalaxyID 15548147, $M_* = 1.2 \times 10^{11}\mathrm{M}_\odot$, $R_{28B} = 62.2$ kpc, $\langle\mu_B\rangle = 26.1$ mag/asec^2. *Top Right:* GalaxyID 16643441, $M_* = 8.1 \times 10^{10}\mathrm{M}_\odot$, $R_{28B} = 56.1$ kpc, $\langle\mu_B\rangle = 25.7$ mag/asec^2. *Bottom Left:* GalaxyID 17668706, $M_* = 4.2 \times 10^{10}\mathrm{M}_\odot$, $R_{28B} = 55.5$ kpc, $\langle\mu_B\rangle = 26.4$ mag/asec^2. *Bottom Right:* GalaxyID 16169302, $M_* = 5.6 \times 10^{10}\mathrm{M}_\odot$, $R_{28B} = 53.3$ kpc, $\langle\mu_B\rangle = 25.7$ mag/asec^2.

B-band images in Figure 11. These images were created using the Monte Carlo radiative transfer code SKIRT (Baes et al. 2003, 2011; Camps & Baes 2015), as described in Appendix A. Note that while we neglect the effects of dust when computing surface brightnesses in this paper, these images include a model for dust extinction. Spiral structure can be seen surrounding the nucleus of each galaxy in Figure 11, consistent with the morphology inferred from $\bar{\epsilon_*}(R_{28B})$.

The largest disk galaxy in our sample has $R_{28B} = 62$ kpc. For comparison, R_{28B} of Malin 1 is ≈ 80 kpc (Boissier et al. 2016), while R_{28B} of UGC1382 is approximately equal to that of our largest galaxy (Hagen et al. 2016). Thus the largest galaxies in our sample have sizes comparable to those of observed giant LSBGs.

The ex-situ stellar mass fractions of the four galaxies in Figure 11 are 0.57, 0.19, 0.27, and 0.33, in order of decreasing R_{28B}, meaning that all four of these galaxies have experienced a significant mass contribution from mergers. In fact, the largest 17 disk galaxies in our sample have $f_{\mathrm{ex-situ}} > 0.1$. However, the largest galaxy with $f_{\mathrm{ex-situ}} < 0.1$ has $R_{28B} = 48$ kpc, so the gap between the sizes of the largest disk galaxies that had a mostly secular evolution and those with substantial mergers is not very large. This may be due to statistics: the box size of EAGLE is not sufficient to host large numbers of massive galaxies with many mergers, so it is unlikely to contain the most unusually large galaxies that can be found in our Universe.

Thus, despite the general tendency of mergers to make galaxies less disk-dominated, some galaxies with significant mass growth from mergers have large extended disks. To examine in more detail the range of possible outcomes of recent mergers, we show in Figure 12 the kinematic evolution of galaxies with different stellar mass contribution from mergers between $z = 0.5$ and $z = 0$. For different bins of $\bar{\epsilon_*}(R_{28B})$ at $z = 0$, we show $\bar{\epsilon_*}$ as a function of radius for the $z = 0$ galaxies and their $z = 0.5$ main progenitors. Galaxies with lower stellar masses at $z = 0$ than $z = 0.5$ have been excluded from the figure as they are generally undergoing stripping as satellites, and this process is likely to affect their kinematic morphology in a unique way. We have also seen in the previous two subsections that LSBGs are unlikely to survive being stripped. We therefore exclude this subset of galaxies from our sample in the remainder of this subsection.

It is apparent in Figure 12 that galaxies with little contribution from mergers have their relative ordering in kinematic morphology largely fixed by $z = 0.5$. Their evolution in $\bar{\epsilon_*}(R)$ varies with galaxy stellar mass. Galaxies with $M_* < 10^{9.8}$ at $z = 0$ have not changed their kinematic profiles significantly since $z = 0.5$, whereas for higher M_*, the buildup of rotationally-supported disks can be seen, consistent with the evolutionary picture presented in Clauwens et al. (2018). Specifically, galaxies become more kinematically disk dominated in their outer parts near R_{28B}.

Looking at the panels in Figure 12 that represent galaxies with a higher merger contribution between $z = 0.5$ and $z = 0$, we see that the correlation between kinematic morphology at these two redshifts becomes weaker as mergers become more important, especially for the lowest-mass galaxies. We note that galaxies are not evenly distributed in number between the different $\bar{\epsilon_*}(R_{28B})$ bins, as galaxies with large mass contributions from mergers are predominantly dispersion-dominated at $z = 0$ (Figure 10). The majority of such galaxies follow the trend shown by the red lines in the bottom panels of Figure 12, decreasing in $\bar{\epsilon_*}$ with time over their full radial extent, and especially at large radii. However, for the highest bin of $\bar{\epsilon_*}(R_{28B})$ at $z = 0$, shown in magenta, galaxies are more rotation-dominated in their outer parts at $z = 0$ than at $z = 0.5$, despite undergoing substantial mergers. This suggests that mergers might in some cases extend the disks of galaxies rather than destroying them.

To explore this idea further, we select galaxies with a significant contribution to their stellar mass from mergers between $z = 0.5$ and $z = 0$, such that at least 25% of their $z = 0$ stellar mass was found within other subhalos after $z = 0.5$ but before $z = 0$ (i.e. $\Delta M_{\mathrm{ex-situ}}/M_*(z = 0) > 0.25$). We then compute the two-dimensional distribution of their stellar particles in projected radius R and orbital circularity ϵ_*, to see how the particles are distributed physically and kinematically. We do this for three different subsets of the $z = 0$ stellar particles: those that were already in the main progenitor galaxy at $z = 0.5$, those that were accreted from other galaxies between $z = 0.5$ and $z = 0$, and those that formed within the main progenitor between $z = 0.5$ and $z = 0$. We also show the original distribution of the star particles in the $z = 0.5$ main progenitor galaxy for comparison.

We compute the aforementioned distributions for galaxies that have extended disks ($\bar{\epsilon_*}(R_{28B}) > 0.5$) and those that do not ($\bar{\epsilon_*}(R_{28B}) < 0.2$), as well as four different $z = 0$

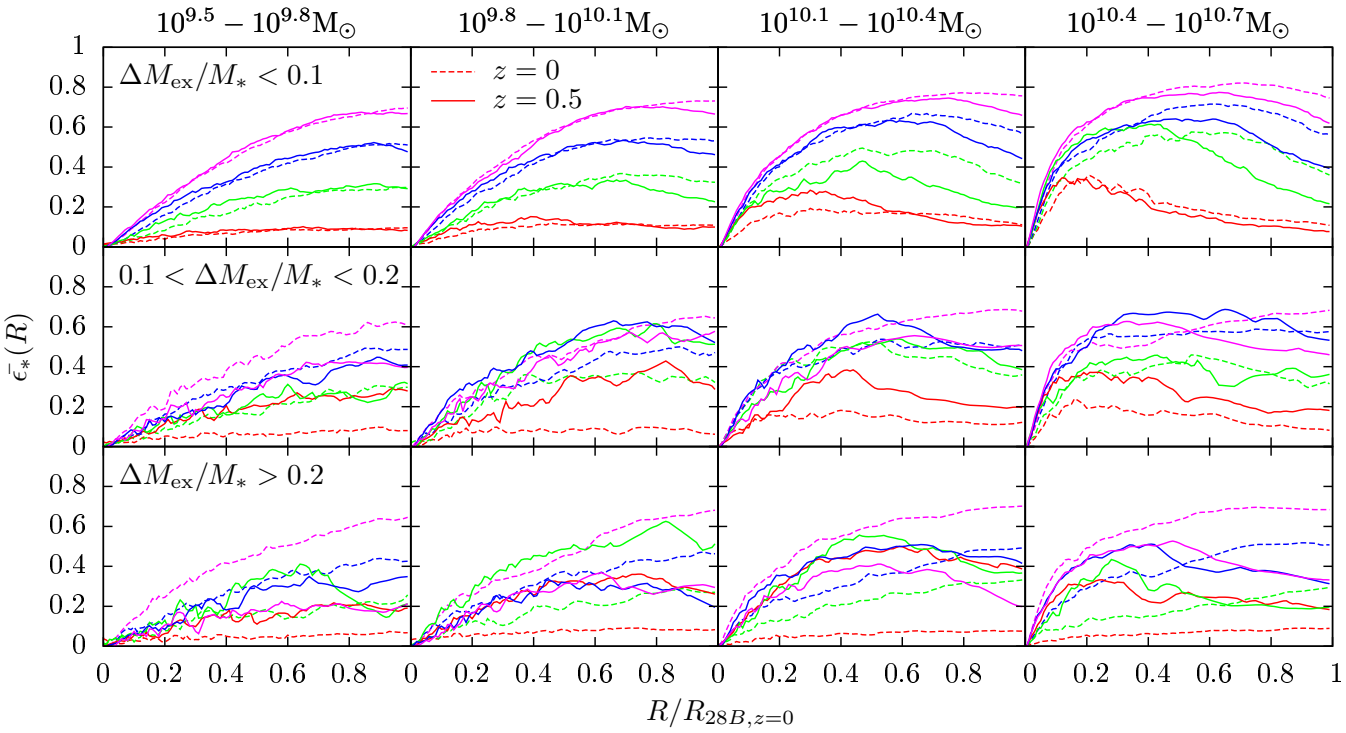

Figure 12. The evolution of $\bar{\epsilon_*}(R)$ (ϵ_* as a function of projected radius) between $z = 0.5$ and $z = 0$ for galaxies with different properties. The columns split galaxies into bins of $z = 0$ stellar mass. The rows show bins in $\Delta M_{\rm ex}/M_*$, the increase in ex-situ stellar mass between $z = 0.5$ and $z = 0$, expressed as a fraction of the total stellar mass at $z = 0$. Galaxies that have lower stellar mass at $z = 0$ than $z = 0.5$ (generally due to stripping while satellites) are excluded from the bins. A limited range of galaxy stellar masses are shown ($M_* < 10^{10.7}$M$_\odot$) in order to select masses at which galaxies exist with a variety of $\Delta M_{\rm ex}/M_*$. In each panel, galaxies are binned into four different ranges of $\bar{\epsilon_*}(R_{28B})$ at $z = 0$: $0 - 0.2$ (red), $0.2 - 0.4$ (green), $0.4 - 0.6$ (blue) and $0.6 - 0.8$ (magenta). Note that different bins of M_* and $\Delta M_{\rm ex}/M_*$ contain significantly different distributions of $\bar{\epsilon_*}(R_{28B})$. Dashed lines represent the median $\bar{\epsilon_*}(R)$ for each bin as a function of R/R_{28B} at $z = 0$. Using the same $z = 0$ physical R_{28B} to scale the radius at $z = 0.5$, the median $\bar{\epsilon_*}(R)$ curve for the main progenitors of the galaxies in each bin is plotted versus R/R_{28B} as solid lines. For galaxies with little contribution from mergers, the relative ordering of $\bar{\epsilon_*}(R_{28B})$ is effectively fixed before $z = 0.5$, whereas for galaxies with a significant merger contribution, there is far more change in the kinematic morphology, with some galaxies becoming more dispersion-dominated but others becoming more rotation-dominated in their outer regions.

stellar mass bins between $10^{9.5}$M$_\odot$ and $10^{11.5}$M$_\odot$. We then obtain the mean fraction of the total $z = 0$ M_* contained in each $(R/R_{28B}, \epsilon_*)$ bin. The particle distributions for the rotation-dominated and dispersion-dominated galaxies are shown in Figure 13 and Figure 14, respectively.

Since the color coding shows the stellar mass in each bin as a fraction of the total $z = 0$ stellar mass of the galaxy, we see that for both dispersion- and rotation-dominated galaxies, the fraction of stellar mass from star formation between $z = 0.5$ and $z = 0$ (bottom row) is higher at lower stellar masses, decreasing from 33% in the lowest mass bin to $\leq 11\%$ in the highest. At fixed stellar mass, however, there is only a small difference between disk and spheroidal galaxies in the fraction of mass gained from star formation. The largest difference occurs in the highest-mass bin, where disk galaxies obtain an average of 11.0% of their $z = 0$ mass from star formation, while for spheroids the fraction is 7.1%. However, the distributions of this value are substantially overlapping: the one-sigma scatter is 6.2% for disk galaxies and 4.1% for spheroids. The difference between spheroid and disk galaxies decreases towards lower masses, such that in the lowest mass bin, the two types of galaxies experience an equal amount of star formation on average.

More significantly different is how the recently-formed stars are distributed in projected radius and orbital circularity. For spheroidal galaxies, the stars form overwhelmingly in the inner regions of the galaxy ($R/R_{28B} < 0.3$), whereas for disk galaxies there is a tail of stars on very cold orbits that extends to $\gtrsim R_{28B}$ visible at the top of the bottom panels in Figure 13.

We split the stars formed in the galaxy into different subgroups depending on whether their parent gas particles entered the main progenitor via mergers or accretion, as well as the redshift at which they became part of the main progenitor. However, we found that the source of the gas does not significantly affect the distribution of the resulting stars in R and ϵ_*, nor does the redshift at which the gas became bound.

In the third row of panels in Figure 13 and Figure 14, we see the distribution of star particles that entered the galaxy via mergers between $z = 0.5$ and $z = 0$. (The fraction of stellar mass from mergers has been chosen to be the same for both disk and spheroidal galaxies.) Again, the distribution

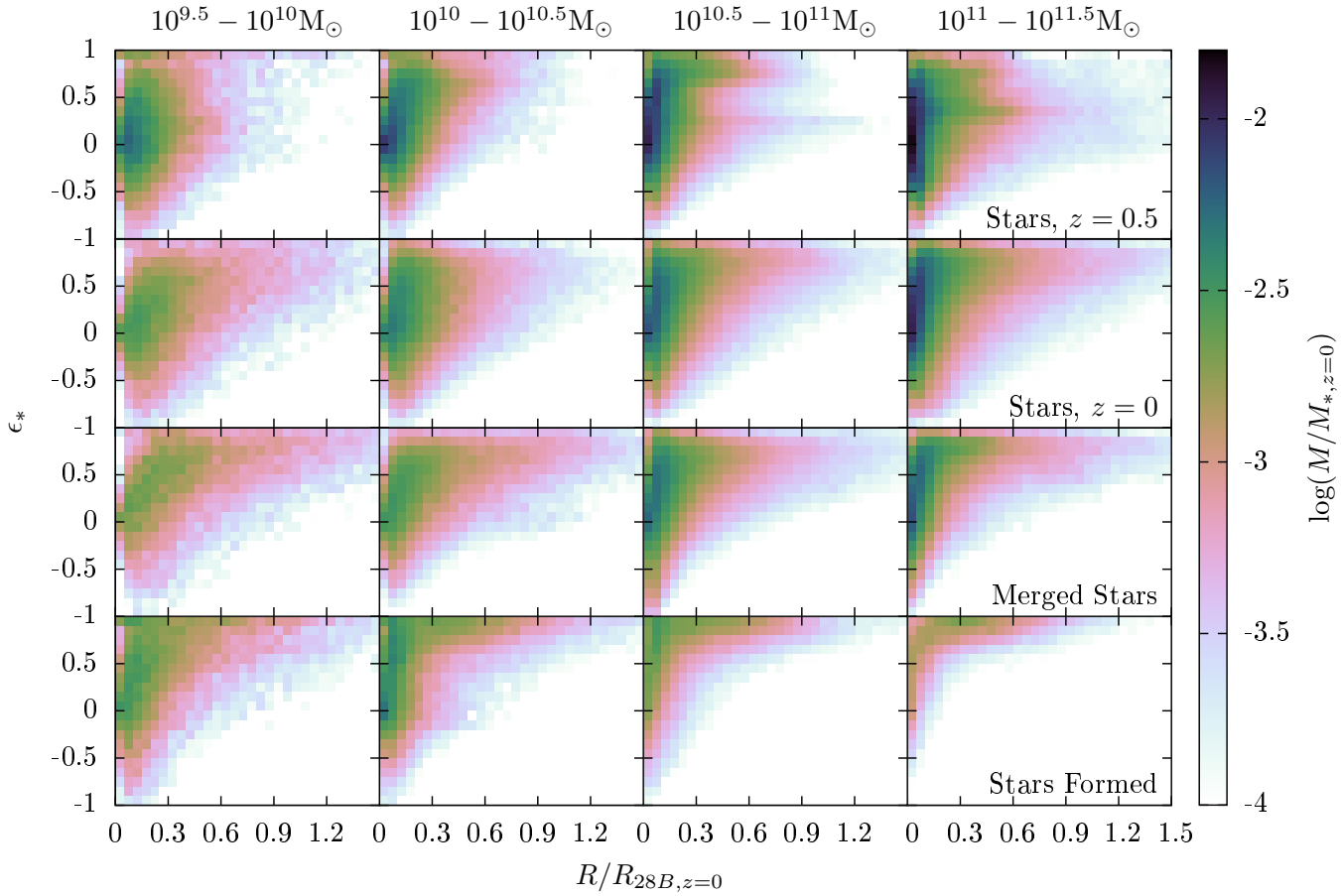

Figure 13. Mean star particle distribution in projected radius R and orbital circularity parameter ϵ_* for galaxies with $\bar{\epsilon_*}(R_{28B}) > 0.5$ at $z = 0$ that gained $> 25\%$ of their $z = 0$ stellar mass from ex-situ stars since $z = 0.5$. Different columns show different bins of $z = 0$ stellar mass. The rows show the distributions of different subsets of stars. All panels show the projected radius scaled by R_{28B} at $z = 0$, with color coding indicating the stellar mass in each bin as a fraction of the $z = 0$ stellar mass of the galaxy. *Top row:* The distribution of the stars in the main progenitor galaxy at $z = 0.5$. *Second row:* The same stellar particles as in the top row, but now their distribution in the descendant galaxy at $z = 0$. Compared to $z = 0.5$, the distribution of stellar particles becomes more kinematically disk-dominated. *Third row:* The ex-situ stars accreted from other galaxies between $z = 0.5$ and $z = 0$. These stars contribute significantly to the outer disk of the galaxy. *Bottom row:* The stars that formed between $z = 0.5$ and $z = 0$ in the main progenitor. Star formation also contributes to the outer disk, especially for lower-mass galaxies.

of these stars is highly different for the selected disk and spheroidal galaxies. For the spheroidal galaxies at $z = 0$, the ex-situ stars are kinematically hot regardless of radius. They predominantly come to inhabit the inner regions of the galaxy, but also form a long tail to R_{28B} and beyond. By comparing the radial distribution of these stars to those in the panels above (second row), which show the $z = 0$ distribution of stars that were already present in the galaxy at $z = 0.5$, we see that the ex-situ stars at large R are building up the stellar halo, especially in the lower-mass bins. This is consistent with the surface density profiles presented in Figure 4.

Conversely, for the galaxies that are kinematically disk-dominated at $z = 0$, the distribution of ex-situ stars that extends to large R has high orbital circularity, although not quite as high as the stars formed since $z = 0.5$. Nevertheless, the mass in stars gained directly from mergers is comparable to or larger than the mass in stars formed since $z = 0.5$ for all the galaxy mass bins presented, implying that ex-situ stars are a large contribution to the highly extended disk seen in our largest LSBGs.

Finally, we examine the top two rows of Figure 13 and Figure 14, showing the distribution at $z = 0.5$ and $z = 0$ of the star particles that have been bound to the galaxies since $z = 0.5$. Because we choose the galaxies presented in the two figures solely based on their $z = 0$ value of $\bar{\epsilon_*}(R_{28B})$, the $z = 0.5$ progenitors of the disk-dominated galaxies are already somewhat more kinematically cold in their outer parts than the progenitors of the spheroidal galaxies (top row). However, the evolution of these star particles increases this difference. For the $z = 0$ spheroidal galaxies, the $z = 0.5$ progenitors initially have a cold rotating component in all mass bins, visible in the top row of panels in Figure 14. However, by $z = 0$, this cold component has essentially disappeared, as seen in the second row of panels. This is the "typical" effect of mergers: to make galaxies more spheroid-dominated. This can be also be inferred from the distribution of morphologies as a function of $f_{\rm ex-situ}$ in Figure 3 and Figure 10.

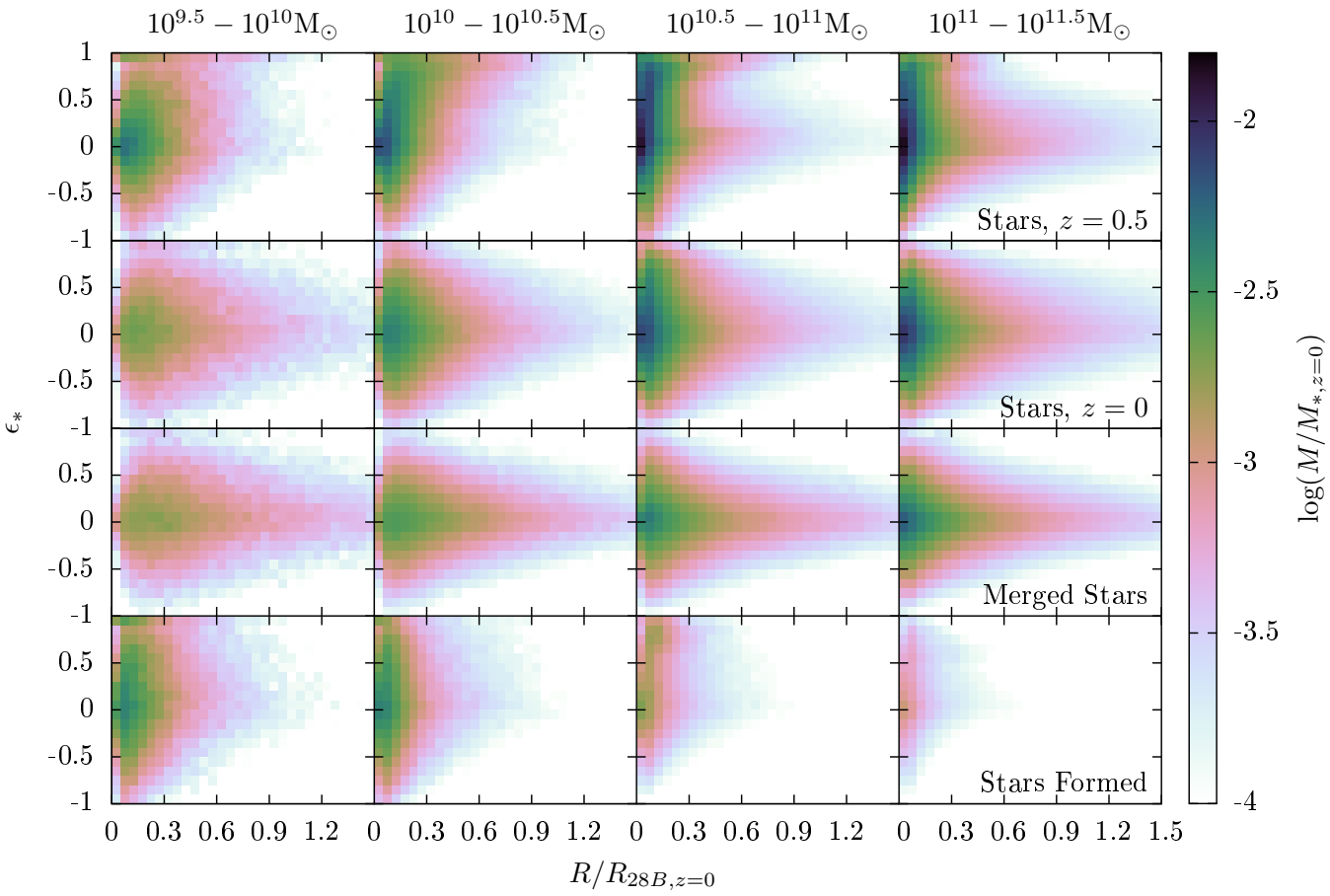

Figure 14. The same as Figure 13, but now for galaxies with $\bar{\epsilon_*}(R_{28B}) < 0.2$ (dispersion-dominated) at $z = 0$ in addition to $\Delta M_{\rm ex-situ}/M_*(z = 0) > 0.25$. A number of differences in the star particle distribution are visible in comparison to Figure 13. The stars present in the main progenitor at $z = 0.5$ become more kinematically spheroid-dominated by $z = 0$. Stars acquired via mergers contribute to a kinematically hot stellar halo in the outer parts of the galaxy rather than a disk, while newly-formed stars do not contribute to the outer parts of the galaxy at all.

However, for the $z = 0$ disk galaxies in Figure 13, the cold component is enhanced in all mass bins.

Thus we can conclude that while mergers do typically transform galaxies into spheroids, there is a subset of mergers that instead builds up a rotationally-supported, extended disk, perhaps leading to the formation of a giant LSBG.

3.6 Comparison to prior work on kinematic evolution due to mergers in EAGLE

The effect of mergers on the kinematics of galaxies in EAGLE has already been studied in Lagos et al. (2018). The authors found that different types of mergers impact the specific angular momentum of galaxies differently. Dry mergers were found to significantly decrease the specific angular momentum of galaxies, whereas wet mergers on average slightly increased it. Moreover, particular types of wet mergers were found to be more likely to spin up the galaxy; these include minor (as opposed to major) mergers, mergers in which the satellite galaxy's spin is aligned with that of the central, and mergers in which the merging satellite has a large orbital angular momentum.

In Lagos et al. (2018), "wet" mergers were defined based on the neutral gas fraction, which we do not compute in this paper, thus precluding a direct comparison. We do note that Lagos et al. (2018) find a larger increase in stellar mass surface density ≈ 1 Gyr after wet mergers than dry ones. This may be consistent with the difference in stellar mass gain from star formation between our kinematic disk and spheroid galaxy samples with $M_* > 10^{10.5}$M$_\odot$. However, at lower stellar masses, there is little difference between the mass in stars formed since $z = 0.5$ in disk and spheroid galaxies. Thus, the influence of wet versus dry mergers is unlikely to fully explain the different angular momentum evolution seen in Figures 13 and 14.

Throughout our paper, we consider any star particles that were once bound to a subhalo other than the main progenitor to be "ex-situ" particles. Lagos et al. (2018), however, define mergers as only those events in which the mass ratio of the two galaxies is at least 1:10, and any smaller mergers are considered "accretion". They also find that accretion tends to increase the angular momentum of galaxies. To check if this affects our results, we broke down the ex-situ contribution to the galaxies in our sample based on the fraction of

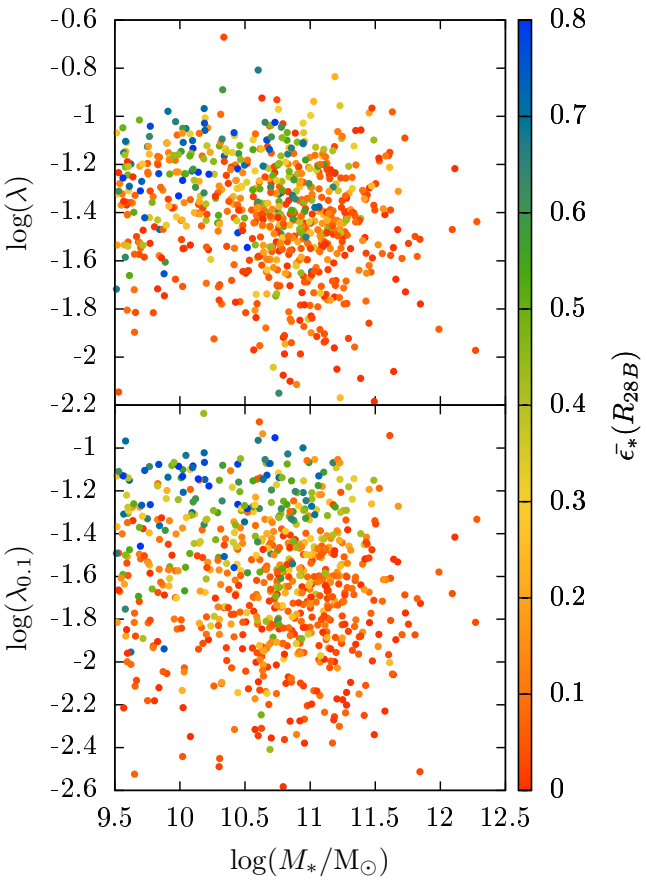

Figure 15. For all central galaxies with $f_{\rm ex-situ} > 0.3$, the galaxy stellar mass (M_*) versus the spin (λ) of the dark matter halo in the dark matter only EAGLE simulation that corresponds to the galaxy's host halo (see §2.4.3 for details). The top panel shows the spin parameter of the entire halo (within r_{200c}) while the lower panel shows the spin only of the inner halo (within $0.1r_{200c}$). Color coding in both panels indicates the local orbital circularity, $\bar{\epsilon}_*$, at R_{28B}. The orbital circularity correlates with the total halo spin, and even more so with the inner halo spin.

ex-situ mass from individual galaxies (i.e., a merger with a more massive galaxy results in more ex-situ stars from that galaxy). We do not find strong differences in the distribution of stellar masses contributed by single objects between the disk and spheroidal subsamples. Therefore, differing mass contributions from accretion, minor, and major mergers are also unlikely to be the main reason for the buildup of disks subsequent to mergers in our sample.

Additionally, Lagos et al. (2018) find an increase in the angular momentum of the outer regions of galaxies (to ≈ 30 kpc) following wet minor mergers with large orbital angular momentum. However, they find that this difference comes from the formation of new stars with high angular momentum at large radii, but not from ex-situ stars gained during the merger. Thus our results appear to depart somewhat from those of Lagos et al. (2018), as we find that both newly-formed stars and ex-situ stars from mergers can contribute to the formation of a large rotationally supported disk.

It is possible that our results differ simply because we are selecting a very unusual subsample of galaxies, whereas Lagos et al. (2018) consider all galaxies that experience mergers. Galaxies with a large fraction of ex-situ stars that also have disky kinematic morphologies are rare, as can be seen in Figure 3 and Figure 10.

One relevant correlation is presented in Figure 15, which plots galaxy stellar mass versus dark matter halo spin parameter, color-coded by $\bar{\epsilon}_*(R_{28B})$, for central galaxies with $f_{\rm ex-situ} > 0.3$. In the upper panel, the spin parameter of the halo is computed within r_{200c}, while in the lower one it is computed within $0.1r_{200c}$. As in Figure 9, the halo properties are those of galaxies' matched host halos in the dark matter only (DMO) run of EAGLE, so they are unaffected by the baryonic physics present in the reference simulation. In the top panel of Figure 15, we see that there exists a correlation between large-scale halo spin and galaxy kinematic morphology. In fact, this correlation is stronger than the one seen for galaxies with low $f_{\rm ex-situ}$ in Figure 9. However, looking at the lower panel, the correlation with the spin of the inner halo is even stronger, such that nearly all galaxies with $\bar{\epsilon}_*(R_{28B}) > 0.5$ have matched DMO halos with the highest inner spin parameters. This is consistent with the results of Zavala et al. (2016), since galaxies that have gained a significant fraction of their mass from mergers are those that formed most of their stars before their halo turnaround time, and according to Zavala et al. (2016) their angular momentum should correlate better with that of the inner dark matter halo.

Given that the DMO halo spins result entirely from the dark matter initial conditions (which determine the accretion to the halo and mergers with other halos over time), the strong correlation between the galaxy angular momentum and the inner halo spin suggests that processes unrelated to baryonic physics are the primary drivers of the angular momentum evolution of galaxies that undergo many mergers. This might also indicate that galaxies that grow their disks from mergers live in unusual large-scale environments. However, we find further exploration of this topic to be beyond the scope of this work.

4 CONCLUSIONS

We examined the formation and evolution of low surface brightness galaxies (LSBGs) and how they differ from high surface brightness galaxies (HSBGs) within the $(100\ {\rm cMpc})^3$ reference run of the EAGLE suite of hydrodynamical cosmological simulations. We computed synthetic B-band surface brightness profiles for galaxies with $M_* > 10^{9.5}{\rm M}_\odot$ using the EAGLE catalog dust-free *ugriz* luminosities (Trayford et al. 2015) of all the star particles bound to each subhalo. We took all galaxies to be in the face-on orientation in order to maximize the number of objects that could potentially be observed as LSBGs if they existed in our Universe.

In order to be able to identify nucleated LSBGs, which are bright in their central regions, we parametrize the "effective" surface brightness via the 28 mag/asec^2 B-band isophote, R_{28B}, and the mean B-band surface brightness within it, $\langle\mu_B\rangle$. For the majority of low-mass galaxies ($M_* \lesssim 10^{10.5}$), $\langle\mu_B\rangle$ separates galaxies into classical LSBG and HSBG subgroups, whose surface brightness profiles can be seen in Figure 5. For this subpopulation, the median surface brightness of galaxies becomes brighter with increasing

stellar mass, as expected. However, galaxies that have had a large mass contribution from mergers (which includes essentially all galaxies with $M_* \gtrsim 10^{11}$) build up a faint stellar halo which increases the size of the 28 mag/asec^2 isophote and thus decreases the mean surface brightness within it (Figure 4). Because of this and the fact that undergoing mergers can significantly alter the evolution of a galaxy, we investigate separately the formation of LSBGs through secular evolution (which is the case for most low-mass LSBGs) and the growth of LSBG disks via mergers (which produces a small number of giant LSBGs). Our main conclusions are as follows:

- Surface brightness in the B band is determined by a combination of the mean surface density of the galaxy, which is related to its physical evolution, and its specific star formation rate, which determines its mass-to-light ratio and can vary on short timescales (Matthee & Schaye 2019). This is shown in Figure 2. The correlation between higher sSFR and higher surface brightness introduces scatter into the correlations between surface brightness and galaxy physical properties that are tightly correlated with stellar mass surface density (Figure 6).

For galaxies that experience predominantly secular growth, which includes the majority of galaxies with $M_* < 10^{10.5}\mathrm{M}_\odot$:

- The mean stellar mass surface density is almost entirely determined by the kinematic morphology and the stellar mass of the galaxy. This can be seen in Figure 3 and Figure 6. This leads to LSBGs generally being highly kinematically disk dominated.
- LSBGs are on average farther from their nearest neighbor galaxy than HSBGs, in agreement with observations. However, we find that this trend is driven entirely by the fact that LSBGs are unlikely to be close-in satellite galaxies (Figure 7). This implies that LSBGs do not form in unusually isolated environments, but rather that they are destroyed by close encounters with massive galaxies.
- LSBGs that are the central galaxy in their host dark matter halo inhabit halos with similar masses and concentrations as those of central HSBGs, although LSBGs tend to have a higher baryon fraction (including both hot and cold gas; Figure 8).
- LSBGs whose evolution was not strongly influenced by mergers appear to form by a combination of the evolutionary processes presented in Zavala et al. (2016) and Clauwens et al. (2018). In this picture of secular galaxy evolution, spheroids form at early times, and disks form around them later from a reservoir of gas that co-rotates with the host dark matter halo. Thus galaxies with high angular momentum tend to be those that formed most of their stars recently, as well as those with higher dark matter halo spins. The correlation between surface brightness and sSFR means that selecting LSBGs selects against young galaxies (Figure 6); however, the correlation between low surface brightness and high dark matter halo spin remains (Figure 8).

Regarding the influence of mergers on galaxy surface brightness profiles and morphologies:

- Mergers generally make galaxies more spheroidal, as can be seen from the fact that nearly all galaxies with large ex-situ fractions are kinematically dispersion-dominated (Figure 3). However, a small subset of galaxies with large ex-situ fractions are kinematically disk-dominated in their faint outer regions (Figure 10). This subset represents some of the largest LSBGs in our sample, such as those shown in Figure 11.
- The ex-situ stars gained from mergers generally build up a faint dispersion-dominated stellar halo component that extends to large radii, as can be seen in the third row of Figure 14. However, in a minority of cases, the stars from mergers can instead build up extended disks, as seen in Figure 13. Merger-related growth is perhaps necessary for the formation of the largest "giant" LSBGs seen in the Universe.
- For galaxies with a high ex-situ stellar mass fraction, the kinematic morphology of their faint outer regions correlates strongly with the spin of the inner part ($< 0.1 r_{200c}$) of their matched dark matter halo from the dark matter only EAGLE run (Figure 15). Given that the dark matter only simulation is unaffected by baryonic physics, this implies that galaxies that grow their disks via mergers may be located in an unusual dark matter environment.

It is possible that we have not identified every mechanism by which low surface brightness galaxies are able to form. However, our results suggest that LSBGs at both low and high masses can form as a result of statistical variation in the processes that also form HSBGs, namely the secular growth of galaxies from gas within their host halo at varying cosmic times, and the buildup of the diffuse outer regions of galaxies due to mergers.

ACKNOWLEDGEMENTS

The authors would like to thank Claudia Lagos for providing data that was used in an early draft of this paper. AK is grateful to Joop Schaye for helpful discussions.

AK, GG, and NP acknowledge support from CONICYT project Basal AFB-170002. GG and NP were supported by Fondecyt 1150300. NP acknowledges support from Fondecyt 1191813.

This work used the DiRAC Data Centric system at Durham University, operated by the Institute for Computational Cosmology on behalf of the STFC DiRAC HPC Facility (www.dirac.ac.uk). This equipment was funded by BIS National E-infrastructure capital grant ST/K00042X/1, STFC capital grant ST/H008519/1, and STFC DiRAC Operations grant ST/K003267/1 and Durham University. DiRAC is part of the National E-Infrastructure.

REFERENCES

Abadi M. G., Navarro J. F., Steinmetz M., Eke V. R., 2003, ApJ, 597, 21
Amorisco N. C., Loeb A., 2016, MNRAS, 459, L51
Baes M. et al., 2003, MNRAS, 343, 1081
Baes M., Verstappen J., De Looze I., Fritz J., Saftly W., Vidal Pérez E., Stalevski M., Valcke S., 2011, ApJS, 196, 22
Baldry I. K. et al., 2012, MNRAS, 421, 621
Barth A. J., 2007, AJ, 133, 1085
Benítez-Llambay A., Frenk C. S., Ludlow A. D., Navarro J. F., 2019, MNRAS, 488, 2387
Boissier S. et al., 2016, A&A, 593, A126

Booth C. M., Schaye J., 2010, MNRAS, 405, L1
Bothun G. D., Impey C. D., Malin D. F., Mould J. R., 1987, AJ, 94, 23
Bothun G. D., Schombert J. M., Impey C. D., Sprayberry D., McGaugh S. S., 1993, AJ, 106, 530
Bruzual G., Charlot S., 2003, MNRAS, 344, 1000
Bullock J. S., Kolatt T. S., Sigad Y., Somerville R. S., Kravtsov A. V., Klypin A. A., Primack J. R., Dekel A., 2001, MNRAS, 321, 559
Burkholder V., Impey C., Sprayberry D., 2001, AJ, 122, 2318
Cañas R., Lagos C. d. P., Elahi P. J., Power C., Welker C., Dubois Y., Pichon C., 2019, arXiv e-prints, arXiv:1908.02945
Camps P., Baes M., 2015, Astronomy and Computing, 9, 20
Camps P., Trayford J. W., Baes M., Theuns T., Schaller M., Schaye J., 2016, MNRAS, 462, 1057
Camps P. et al., 2018, ApJS, 234, 20
Carleton T., Errani R., Cooper M., Kaplinghat M., Peñarrubia J., Guo Y., 2019, MNRAS, 485, 382
Chabrier G., 2003, PASP, 115, 763
Chan T. K., Kereš D., Wetzel A., Hopkins P. F., Faucher-Giguère C. A., El-Badry K., Garrison-Kimmel S., Boylan-Kolchin M., 2018, MNRAS, 478, 906
Clauwens B., Schaye J., Franx M., Bower R. G., 2018, MNRAS, 478, 3994
Cleveland W. S., 1979, Journal of the American Statistical Association, 74, 829
Correa C. A., Schaye J., Clauwens B., Bower R. G., Crain R. A., Schaller M., Theuns T., Thob A. C. R., 2017, MNRAS, 472, L45
Crain R. A. et al., 2015, MNRAS, 450, 1937
Cullen L., Dehnen W., 2010, MNRAS, 408, 669
Dalcanton J. J., Spergel D. N., Gunn J. E., Schmidt M., Schneider D. P., 1997a, AJ, 114, 635
Dalcanton J. J., Spergel D. N., Summers F. J., 1997b, ApJ, 482, 659
Dalla Vecchia C., Schaye J., 2012, MNRAS, 426, 140
Davis M., Efstathiou G., Frenk C. S., White S. D. M., 1985, ApJ, 292, 371
de Blok W. J. G., McGaugh S. S., van der Hulst J. M., 1996, MNRAS, 283, 18
de Blok W. J. G., van der Hulst J. M., 1998, A&A, 335, 421
De Lucia G., Blaizot J., 2007, MNRAS, 375, 2
Dehnen W., Aly H., 2012, MNRAS, 425, 1068
Di Cintio A., Brook C. B., Dutton A. A., Macciò A. V., Obreja A., Dekel A., 2017, MNRAS, 466, L1
Di Cintio A., Brook C. B., Macciò A. V., Dutton A. A., Cardona-Barrero S., 2019, MNRAS, 486, 2535
Dolag K., Borgani S., Murante G., Springel V., 2009, MNRAS, 399, 497
Du W., Cheng C., Wu H., Zhu M., Wang Y., 2019, MNRAS, 483, 1754
Du W., Wu H., Lam M. I., Zhu Y., Lei F., Zhou Z., 2015, AJ, 149, 199
Dubois Y. et al., 2014, MNRAS, 444, 1453
Durier F., Dalla Vecchia C., 2012, MNRAS, 419, 465
Elagali A., Lagos C. D. P., Wong O. I., Staveley-Smith L., Trayford J. W., Schaller M., Yuan T., Abadi M. G., 2018, MNRAS, 481, 2951
Ferland G. J., Korista K. T., Verner D. A., Ferguson J. W., Kingdon J. B., Verner E. M., 1998, PASP, 110, 761
Furlong M. et al., 2017, MNRAS, 465, 722
Furlong M. et al., 2015, MNRAS, 450, 4486
Galaz G., Herrera-Camus R., Garcia-Lambas D., Padilla N., 2011, ApJ, 728, 74
Galaz G., Milovic C., Suc V., Busta L., Lizana G., Infante L., Royo S., 2015, ApJ, 815, L29
Galaz G., Villalobos A., Infante L., Donzelli C., 2006, AJ, 131, 2035
Genel S. et al., 2014, MNRAS, 445, 175
Groves B., Dopita M. A., Sutherland R. S., Kewley L. J., Fischera J., Leitherer C., Brandl B., van Breugel W., 2008, ApJS, 176, 438
Haardt F., Madau P., 2001, in Clusters of Galaxies and the High Redshift Universe Observed in X-rays, Neumann D. M., Tran J. T. V., eds.
Hagen L. M. Z. et al., 2016, ApJ, 826, 210
Heyer M. H., Carpenter J. M., Snell R. L., 2001, ApJ, 551, 852
Hoffman Y., Silk J., Wyse R. F. G., 1992, ApJ, 388, L13
Hopkins P. F., 2013, MNRAS, 428, 2840
Impey C., Bothun G., 1989, ApJ, 341, 89
Impey C., Bothun G., 1997, ARA&A, 35, 267
Impey C., Burkholder V., Sprayberry D., 2001, AJ, 122, 2341
Jiang L., Helly J. C., Cole S., Frenk C. S., 2014, MNRAS, 440, 2115
Jimenez R., Padoan P., Matteucci F., Heavens A. F., 1998, MNRAS, 299, 123
Jonsson P., Groves B. A., Cox T. J., 2010, MNRAS, 403, 17
Katsianis A. et al., 2017, MNRAS, 472, 919
Katz H., Lelli F., McGaugh S. S., Di Cintio A., Brook C. B., Schombert J. M., 2017, MNRAS, 466, 1648
Kaviraj S. et al., 2017, MNRAS, 467, 4739
Kennicutt, Jr. R. C., 1998, ApJ, 498, 541
Koda J., Yagi M., Yamanoi H., Komiyama Y., 2015, ApJ, 807, L2
Lagos C. d. P. et al., 2018, MNRAS, 473, 4956
Leisman L. et al., 2017, ApJ, 842, 133
Lelli F., Fraternali F., Sancisi R., 2010, A&A, 516, A11
Lelli F., McGaugh S. S., Schombert J. M., 2016, AJ, 152, 157
Mapelli M., Moore B., Ripamonti E., Mayer L., Colpi M., Giordano L., 2008, MNRAS, 383, 1223
Martin G. et al., 2019, MNRAS, 485, 796
Matthee J., Schaye J., 2019, MNRAS, 484, 915
Matthee J., Schaye J., Crain R. A., Schaller M., Bower R., Theuns T., 2017, MNRAS, 465, 2381
Mayer L., Wadsley J., 2004, MNRAS, 347, 277
McAlpine S. et al., 2016, Astronomy and Computing, 15, 72
McGaugh S. S., 1994, ApJ, 426, 135
Merritt A., van Dokkum P., Danieli S., Abraham R., Zhang J., Karachentsev I. D., Makarova L. N., 2016, ApJ, 833, 168
Mihos J. C. et al., 2015, ApJ, 809, L21
Minchin R. F. et al., 2004, MNRAS, 355, 1303
Mo H. J., McGaugh S. S., Bothun G. D., 1994, MNRAS, 267, 129
Moran S. M. et al., 2012, ApJ, 745, 66
Muñoz R. P. et al., 2015, ApJ, 813, L15
Noguchi M., 2001, MNRAS, 328, 353
Oman K. A., Marasco A., Navarro J. F., Frenk C. S., Schaye J., Benítez-Llambay A. r., 2019, MNRAS, 482, 821
Oman K. A. et al., 2015, MNRAS, 452, 3650
Papastergis E., Adams E. A. K., Romanowsky A. J., 2017, A&A, 601, L10
Peñarrubia J., McConnachie A., Babul A., 2006, ApJ, 650, L33
Pickering T. E., Impey C. D., van Gorkom J. H., Bothun G. D., 1997, AJ, 114, 1858
Pillepich A. et al., 2018, MNRAS, 473, 4077
Planck Collaboration et al., 2014, A&A, 571, A16
Prada F., Klypin A. A., Cuesta A. J., Betancort-Rijo J. E., Primack J., 2012, MNRAS, 423, 3018
Price D. J., 2008, Journal of Computational Physics, 227, 10040
Prole D. J., van der Burg R. F. J., Hilker M., Davies J. I., 2019, MNRAS, 488, 2143
Qu Y. et al., 2017, MNRAS, 464, 1659
Román J., Trujillo I., 2017a, MNRAS, 468, 703
Román J., Trujillo I., 2017b, MNRAS, 468, 4039
Rong Y., Guo Q., Gao L., Liao S., Xie L., Puzia T. H., Sun S., Pan J., 2017, MNRAS, 470, 4231
Rosas-Guevara Y., Bower R. G., Schaye J., McAlpine S., Dalla

Vecchia C., Frenk C. S., Schaller M., Theuns T., 2016, MNRAS, 462, 190
Rosenbaum S. D., Bomans D. J., 2004, A&A, 422, L5
Rosenbaum S. D., Krusch E., Bomans D. J., Dettmar R. J., 2009, A&A, 504, 807
Sánchez S. F. et al., 2013, Astronomy and Astrophysics, 554, A58
Sandage A., Binggeli B., 1984, AJ, 89, 919
Santos-Santos I. M., Di Cintio A., Brook C. B., Macciò A., Dutton A., Domínguez-Tenreiro R., 2018, MNRAS, 473, 4392
Schaller M., Dalla Vecchia C., Schaye J., Bower R. G., Theuns T., Crain R. A., Furlong M., McCarthy I. G., 2015a, MNRAS, 454, 2277
Schaller M. et al., 2015b, MNRAS, 451, 1247
Schaye J., 2004, ApJ, 609, 667
Schaye J. et al., 2015, MNRAS, 446, 521
Schaye J., Dalla Vecchia C., 2008, MNRAS, 383, 1210
Shen S., Mo H. J., White S. D. M., Blanton M. R., Kauffmann G., Voges W., Brinkmann J., Csabai I., 2003, MNRAS, 343, 978
Springel V., 2005, MNRAS, 364, 1105
Springel V., Di Matteo T., Hernquist L., 2005, MNRAS, 361, 776
Springel V., White S. D. M., Tormen G., Kauffmann G., 2001, MNRAS, 328, 726
Swaters R. A., Madore B. F., Trewhella M., 2000, ApJ, 531, L107
Thob A. C. R. et al., 2019, MNRAS, 485, 972
Trayford J. W. et al., 2017, MNRAS, 470, 771
Trayford J. W., Frenk C. S., Theuns T., Schaye J., Correa C., 2019, MNRAS, 483, 744
Trayford J. W., Schaye J., 2019, MNRAS, 485, 5715
Trayford J. W., Theuns T., Bower R. G., Crain R. A., Lagos C. d. P., Schaller M., Schaye J., 2016, MNRAS, 460, 3925
Trayford J. W. et al., 2015, MNRAS, 452, 2879
Tremonti C. A. et al., 2004, ApJ, 613, 898
van den Hoek L. B., de Blok W. J. G., van der Hulst J. M., de Jong T., 2000, A&A, 357, 397
van der Burg R. F. J. et al., 2017, A&A, 607, A79
van der Hulst J. M., Skillman E. D., Smith T. R., Bothun G. D., McGaugh S. S., de Blok W. J. G., 1993, AJ, 106, 548
van Dokkum P. et al., 2019, ApJ, 880, 91
van Dokkum P. G., Abraham R., Merritt A., Zhang J., Geha M., Conroy C., 2015a, ApJ, 798, L45
van Dokkum P. G. et al., 2015b, ApJ, 804, L26
Vogelsberger M. et al., 2014, MNRAS, 444, 1518
Wang L., Dutton A. A., Stinson G. S., Macciò A. V., Penzo C., Kang X., Keller B. W., Wadsley J., 2015, MNRAS, 454, 83
Wechsler R. H., Bullock J. S., Primack J. R., Kravtsov A. V., Dekel A., 2002, ApJ, 568, 52
Wiersma R. P. C., Schaye J., Smith B. D., 2009a, MNRAS, 393, 99
Wiersma R. P. C., Schaye J., Theuns T., Dalla Vecchia C., Tornatore L., 2009b, MNRAS, 399, 574
Wyder T. K. et al., 2009, ApJ, 696, 1834
Zaritsky D. et al., 2019, ApJS, 240, 1
Zavala J. et al., 2016, MNRAS, 460, 4466
Zhu Q. et al., 2018, MNRAS, 480, L18
Zubko V., Dwek E., Arendt R. G., 2004, ApJS, 152, 211

APPENDIX A: IMPACT OF DUST ON SURFACE BRIGHTNESS

All B-band surface brightnesses presented in the main body of this paper were computed using dust-free luminosities for the EAGLE stellar particles. In this appendix, we estimate the effect of dust on these surface brightness values using images produced with the Monte Carlo radiative transfer code SKIRT (Baes et al. 2003, 2011; Camps & Baes 2015). Only a full radiative transfer analysis can properly take into account the relative distribution of stars and dust in each galaxy when estimating the dust obscuration.

We use the 60 pkpc per side u and g band images created for the EAGLE catalog for galaxies with $M_* > 10^{10}\mathrm{M}_\odot$, and also supplement these with newly created images for galaxies with lower masses and $R_{28B} > 30$ pkpc. The full details of the SKIRT modeling used for both the EAGLE catalog and our new images can be found in Trayford et al. (2017). Here we provide a brief summary.

The inputs to SKIRT for each galaxy are the spatial distribution of emitted stellar light and the dust distribution. The former is computed similarly as in Trayford et al. (2015). Each stellar particle older than 100 Myr is assumed to be described by a simple stellar population, for which the initial particle mass, stellar age, and SPH smoothed metallicity are used to compute a GALAXEV Bruzual & Charlot (2003) spectral energy distribution (SED), assuming a Chabrier (2003) initial mass function. The mass resolution of EAGLE is such that young stellar populations are poorly sampled. Thus, star-forming gas particles and stellar particles younger than 100 Myr are "re-sampled": their associated stellar mass is subdivided into stellar populations with mass distribution based on the observed mass function of Milky Way molecular clouds (Heyer et al. 2001), and each subpopulation is stochastically assigned a formation time based on the star formation rate of the parent gas particle. Subpopulations older than 10 Myr are assigned GALAXEV SEDs. Stellar populations younger than 10 Myr are assigned MAPPINGS-III (Groves et al. 2008) SEDs, which include a prescription for dust absorption within (unresolved) stellar birth clouds based on Jonsson et al. (2010). Spatial smoothing is then applied to the star particles to produce a continuous spatial luminosity distribution for the galaxy.

The dust spatial distribution is computed assuming that dust traces the distribution of cold, metal-rich gas. The dust-to-metal ratio is taken to be constant:

$$f_{\mathrm{dust}} = \frac{\rho_{\mathrm{dust}}}{Z\rho_{\mathrm{gas}}} = 0.3, \tag{A1}$$

where ρ_{gas} is the density of gas that is either star forming or has $T < 8000$ K, and Z is its metallicity. This value of f_{dust} was chosen such that applying it to the population of EAGLE galaxies reproduces FIR observations (Camps et al. 2016). The dust model of Zubko et al. (2004) is assumed, and the dust optical depth is computed over an adaptively defined (AMR) grid.

Using these inputs, SKIRT produces a mock IFU image of each galaxy, assuming a given galaxy orientation and distance from the detector. We utilize the u and g band images originally made by Trayford et al. (2017), which are 60 pkpc on a side with resolution (pixel size) of 0.23 kpc, and were created for all galaxies with $M_* > 10^{10}\mathrm{M}_\odot$. We convert these images to the B band using the same equation from Lupton (2005) as in the body of the paper (Eqn. 1). We have also produced the following additional images in the B-band:

- images of galaxies with $10^{9.5} < M_*/\mathrm{M}_\odot < 10^{10}$, with size 90 pkpc per side in order to encompass R_{28B} for all galaxies at these masses;
- images with size 300 pkpc per side, for those galaxies with $M_* > 10^{10}\mathrm{M}_\odot$ and $R_{28B} \gtrsim 30$ pkpc.

Because radiative transfer is computationally expensive, we used a resolution for these images lower than that of the EAGLE catalog images, with pixel size 0.94 pkpc. To further decrease the processing time, we only created new images for those galaxies with a substantial amount of dust, as other galaxies are expected to be minimally affected by dust extinction. We use the dust resolution criterion defined by Camps et al. (2018): $N_{\rm dust} > 250$ in the EAGLE catalog, where $N_{\rm dust}$ is the number of "dust particles", defined as the larger of the number of star forming gas particles and the number of cold gas particles. Camps et al. (2018) determined that galaxies following this criterion generally have well-resolved spatial dust distributions that can be used by SKIRT. Thus the results shown in this appendix are only for those galaxies that contain significant amounts of dust.

In the body of the paper, we measure the surface brightnesses of all galaxies in the face-on orientation, based on the eigenvectors of the moment-of-inertia tensor. We similarly choose SKIRT images that are oriented "face-on"; however, EAGLE catalog "face-on" SKIRT images are oriented with the angular momentum of the galaxy's stellar component towards the line of sight. We thus recompute our dust-free particle-based surface brightness values with the galaxies oriented based on their angular momentum vector. For disk galaxies, the minor axis and the direction of the spin vector are generally well aligned, but some elliptical galaxies are prolate and rotate about their major axis (Thob et al. 2019). While the latter galaxies are also old and not expected to contain a significant amount of dust, we nevertheless note that for a small minority of galaxies presented in this appendix, the impact of dust may be overestimated relative to what it would be for the galaxy orientation presented in the body of the paper.

From the mock IFU image created by SKIRT, we can measure R_{28B} and $\langle\mu_B\rangle$. Measuring these parameters from a mock image is inherently somewhat different than doing so using discrete stellar particles. We adopt a method that is intended to be similar to the manner in which we obtain these parameters from the particle data. We assume that the isophotes of the galaxy are ellipses that have equal orientation and axis ratio throughout the image, as we do for the particles. These are obtained by finding the direction of maximum variance in the image, and taking the square root of the ratio of this variance to the variance in the perpendicular direction. We then compute the mean local surface brightness in elliptical annuli with this orientation and axis ratio and find the one that has a value of 28 mag/asec^2, taking that smallest such annulus if there is more than one. This determines R_{28B}. We then simply compute the mean surface brightness within R_{28B} to obtain $\langle\mu_B\rangle$.

By nature, $\langle\mu_B\rangle$ is highly dependent on R_{28B} for a galaxy of fixed total luminosity. The finite spatial resolution of SKIRT images imposes some "smoothing" on the surface brightness profiles derived from them, as does the kernel smoothing of individual particles represented by Monte Carlo sampling. This means that, while one would expect R_{28B} to be the same or smaller when computed with dust extinction than without, this is sometimes not the case, and R_{28B} measured from the SKIRT image can be somewhat larger than that measured from the non-extincted star particles.

We are able to quantify the effect of differing SKIRT image resolutions by using a subsample of galaxies with $R_{28B} \approx 30$ pkpc whose radii we measure in both the original EAGLE images (with resolution 0.23 pkpc) and in the larger 300 pkpc B-band images we have created that have a resolution of 0.94 pkpc. We find that R_{28B} measured from the latter images is on average 4% larger than that measured from the former, and $\langle\mu_B\rangle$ is correspondingly 0.08 mag/asec^2 larger. Additionally, the one sigma scatter between the values of R_{28B} and $\langle\mu_B\rangle$ measured at the two resolutions is 4% and $\pm$0.08 mag/asec^2, respectively. Given that the size of the uncertainty on $\langle\mu_B\rangle$ measured from the star particles is 0.1 mag/asec^2 (§3.1), the difference in resolution between the two subsets of SKIRT images used in this appendix should not have a significant effect our conclusions.

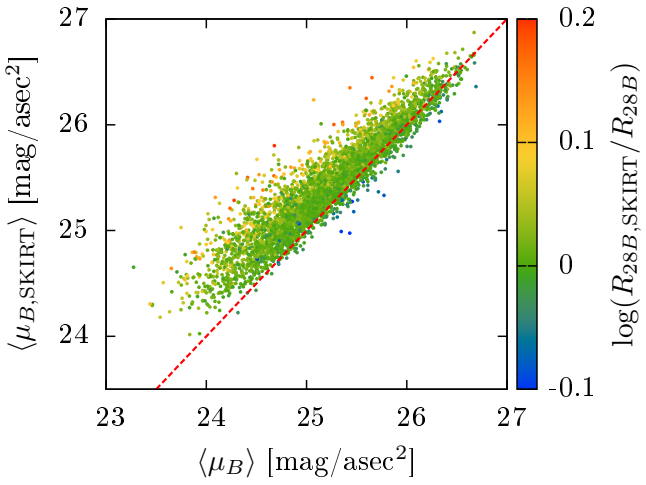

Figure A1. $\langle\mu_B\rangle$, the dust-free surface brightness within the 28 mag/asec^2 B-band isophote computed from the EAGLE stellar particles, versus $\langle\mu_{B,\rm SKIRT}\rangle$, the equivalently-defined surface brightness measured from the SKIRT images including dust extinction. The only galaxies shown from our sample are those that contain sufficient dust to accurately resolve its distribution (see text for criteria). The red dashed line marks the line of equality. Color coding represents the ratio of the 28 mag/asec^2 B-band isophotal radius measured from the SKIRT image to that measured from the star particles.

4415 of 6987 galaxies in our sample contain sufficient dust that we measure their R_{28B} and $\langle\mu_B\rangle$ in dust-extincted SKIRT images. In Figure A1, we show $\langle\mu_B\rangle$ as measured from the dust-free EAGLE particles versus $\langle\mu_{B,\rm SKIRT}\rangle$ measured from the SKIRT image including dust extinction. The color coding shows the ratio of R_{28B} measured from the SKIRT image ($R_{28B,\rm SKIRT}$) to that measured from the EAGLE particles. $\langle\mu_{B,\rm SKIRT}\rangle$ is on average 0.22 mag/asec^2 fainter than $\langle\mu_B\rangle$ from the particles. However, we see that there is a trend such that bright galaxies are more strongly affected by dust extinction than faint ones. The effect is nevertheless not strong enough to greatly change the relative ordering of galaxies by surface brightness. There are a small number of visible outliers for which $\langle\mu_B\rangle$ from SKIRT is much fainter than that from the particles. Visual inspection of the SKIRT images reveals that these galaxies generally have large amounts of dust extinction (visible as dust lanes) in their bright nuclear regions. This decreases the mean surface brightness within R_{28B}.

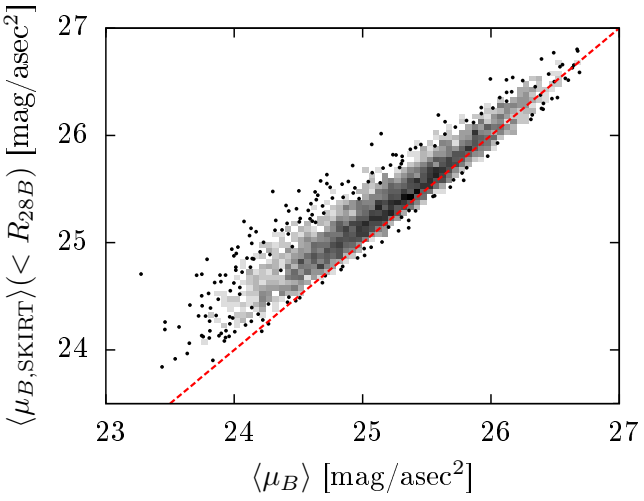

Figure A2. Similar to Figure A1, but now showing $\langle \mu_{B,\mathrm{SKIRT}} \rangle$ measured within the same size radial aperture (R_{28B}) as was used to measure $\langle \mu_B \rangle$ from the EAGLE star particles. The shading of each bin represents the log-number of points within; bins with only one point are represented by the individual point. We note that the stochasticity inherent to Monte Carlo radiative transfer means that the surface brightness derived from SKIRT will sometimes be slightly brighter than that derived from the EAGLE particles for galaxies whose dust extinction is close to zero.

We can also see in Figure A1 that there is a correlation between the difference between $\langle \mu_{B,\mathrm{SKIRT}} \rangle - \langle \mu_B \rangle$ and $R_{28B,\mathrm{SKIRT}}/R_{28B}$. For the majority of galaxies, the value of R_{28B} measured from the SKIRT images and the star particle distribution is similar. Extinction in the outer parts of the galaxy can cause R_{28B} to be smaller in the SKIRT images, making the galaxy appear more compact and its $\langle \mu_{B,\mathrm{SKIRT}} \rangle$ brighter. However, cases in which R_{28B} in the SKIRT images is larger than that measured from the particles are likely the result of the finite resolution and shot noise in the SKIRT images.

To ensure that our estimate of the dust extinction is not highly biased by these effects, we also compute $\langle \mu_{B,\mathrm{SKIRT}} \rangle$ within the same R_{28B} used to measure $\langle \mu_B \rangle$ from the particles. This is shown in Figure A2. The distribution of $\langle \mu_{B,\mathrm{SKIRT}} \rangle$ in this figure is similar to that in Figure A1, implying that the majority of the effect seen there is due to dust extinction within R_{28B} rather than the measured value of the latter. The galaxies in Figure A2 are on average 0.18 mag/asec^2 fainter with dust extinction than without; however, this value decreases from 0.51 mag/asec^2 for galaxies with (dust-free) $23.5 < \langle \mu_B \rangle < 24$ to 0.05 mag/asec^2 for galaxies with $26 < \langle \mu_B \rangle < 26.5$.

We repeat that the galaxies shown in Figures A1 and A2 are only those that contain a substantial amount of dust. In particular, all galaxies shown in these figures have non-zero star formation rates, whereas many of the galaxies in our sample do not (Figure 2); this is due to the assumptions made about the dust distribution following that of the star-forming/cold gas. Dust thus has the effect of slightly lowering the influence of SFR on the surface brightness (seen in Figure 2). However, the difference is significantly smaller than that caused by the SFR itself: the brightest galaxies are made fainter by ≈ 0.5 mag/asec^2, whereas their SFR increases their brightness relative to a passive galaxy by ≈ 1.5 mag/asec^2.

The Spearman correlation coefficient between $\langle \mu_B \rangle$ and $\langle \mu_{B,\mathrm{SKIRT}} \rangle$ for galaxies with substantial dust is 0.93 with separately measured R_{28B} and 0.96 within the same R_{28B}. If we assume galaxies without substantial dust have $\langle \mu_B \rangle$ equal to $\langle \mu_{B,\mathrm{SKIRT}} \rangle$ (which we find to be approximately true for those dust-free galaxies that have EAGLE u and g SKIRT images), these correlation coefficients remain unchanged. Overall, the effect of dust on the surface brightness is small for the majority of galaxies and does not significantly affect the relative ordering of galaxies in terms of their surface brightness. This is partly because we take all galaxies to be face-on, which is the orientation that minimizes the dust extinction. We thus assume that it is justified to ignore the effect of dust in the body of this paper.